B₀ Shimming using Pyrolytic Graphite





Thesis

submitted in partial fulfillment of the requirements for the degree of

MASTER in PHYSICS

Author:

Supervisor at LION:

Prof. dr. ir. T.H. Oosterkamp

Supervisors at LUMC:

Prof. dr. A.G. Webb

Dr. ir. W.M. Brink

Leiden, The Netherlands, July 8, 2017



B_0 Shimming using Pyrolytic Graphite

Andrea Peña

Huygens-Kamerlingh Onnes Laboratory, Leiden University P.O. Box 9500, 2300 RA Leiden, The Netherlands 8^{th} July 2017

Abstract

 B_0 magnetic field non-uniformity is the cause of a large amount of image artifacts in MRI. B_0 inhomogeneities arise due to magnetic susceptibility differences between tissues. In particular, the 9 ppm magnetic susceptibility difference between air and tissue generate disturbances in the B_0 main field near the skin. We study the B_0 passive shimming approach of covering the skin with a susceptibility-matching material from both an experimental and a mathematical viewpoint. In the experimental study, a lightweight and simple to shape pyrolytic graphite composite foam is used to compensate for the field inhomogeneities in the region of the neck. We experimentally demonstrate that the pyrolytic graphite foam improves the uniformity of the static field in a phantom and in vivo at 3T. In the numerical study, we aim for a design of a neck shim which efficiently homogenizes the B_0 field while being practically implementable. We propose a level set optimization method as an approach to find the optimum design for a neck shim. Simulations prove that the proposed method is able to solve the topological optimization problem while preserving the imposed constraints.

Contents

1	\mathbf{Intr}	oducti	on	8
	1.1		ation	8
	1.2	Goal		9
	1.3	Thesis	Outline	10
2	\mathbf{Pre}	limina	ries	11
	2.1	Basic	Principles of MRI	11
	2.2	B_0 Sh	imming	15
	2.3	B_0 field	d mapping	18
3	\mathbf{PG}	Foam	for B_0 Passive Shimming: an Experimental Study	19
	3.1		ů i	19
		3.1.1	Magnetic Susceptibility of PG foam	20
		3.1.2	Electrical Conductivity of the PG foam	21
	3.2	Mater	ials and Methods	21
		3.2.1	PG foam construction	22
		3.2.2	SNR	22
		3.2.3	Phantom	23
		3.2.4	PG foam neck shim	23
	3.3	Result	s and Discussion	24
		3.3.1	SNR	24
		3.3.2	PG foam characterization	26
		3.3.3	In vivo Experiments	29
4	Opt	imum	PG Foam Design: a Numerical Study	33
	4.1^{-1}		· · · · · · · · · · · · · · · · · · ·	33
		4.1.1	B_0 modeling: the forward problem	34
		4.1.2	Inverse Problem Framework	35
		4.1.3	Gradient Descent Algorithm	36
		4.1.4	Level Set Methodology Integrated into a Gradient Descent Algorithm	37
		4.1.5	Subdomains to increase the speed of the algorithm	
	4.2	Result	s and Discussion	

5 Summary and Conclusion	52
Appendix A	53
Acknowledgements	55
Bibliography	56

Chapter 1

Introduction

Magnetic Resonance Imaging (MRI) is a compelling medical imaging technique which offers a wide range of applications in medical diagnosis. Worldwide there are estimated to be 36000 MRI scanners [1]. This imaging technique was first described by Peter Lauterbur in 1973 [2]. Since then, MRI has been proven to be a very useful imaging technique as it is capable of producing detailed spatial images and physical and chemical data while being harmless for the patient.

MRI is based on the physical phenomenon of nuclear magnetic resonance (NMR). In the presence of an applied magnetic field certain nuclei can absorb and re-emit electromagnetic energy. Most MRI scanners image the nucleus of the proton in the hydrogen atoms because these atoms exist in abundance in biological tissues, predominantly, in the form of water and fat. The main static magnetic field, known as the B_0 field, aligns the hydrogen nuclei in the body and pulses of radio waves are used to excite the nuclear spin energy transition. Magnetic field gradients localize the signal in space by spatial encoding of the spins. The biophysical surroundings of each tissue cause different movement characteristics of the protons which provides 'tissue contrast'. Thus, MRI relies on the differences in the physical properties of protons in the water molecules to distinguish one tissue from another.

1.1 Motivation

In many clinical and research MRI methods, the uniformity of the B_0 main field is crucial for image signal and contrast. However, obtaining a fully homogeneous field is still a challenging issue. Perturbations of the field mostly arise due to differences in magnetic susceptibilities between tissues. In particular, the 9 ppm (ppm stands for parts per million) susceptibility difference between air and tissue causes considerable B_0 inhomogeneities near the skin and near the lungs. The image gets distorted and signal is lost leading to artifacts such as unreliable fat suppression, intravoxel dephasing, blurring and geometrical distortions.

The process by which the main magnetic field is made more uniform is called B_0 shimming.

In this thesis, we focus on a passive shimming approach which relies on covering the skin with a tissue susceptibility-matched material. In this way, the field inhomogeneities in region of interest (ROI) are corrected. In this project, we aim to improve the homogeneity of the B_0 magnetic field in the region of the neck and shoulders. Due to the difference in magnetic susceptibility of tissue types and materials around the neck (especially the airtissue interface), achieving an artifact-free image of the neck and shoulder region is very difficult. Compensating for the perturbations generated around the skin is essential for clinical applications. For example, a homogeneous B_0 field around this region could lead to an artifact-free imaging of the brachial plexus, which is a network of nerves extending from the spinal cord to the armpit. Magnetic Resonance Neurography (MRN), which is a powerful technique to image the nerves, provides information about the internal state of the nerve facilitating diagnosis and monitoring diseases affecting the brachial plexus [3–5]. Eliminating the sample-induced inhomogeneities around the neck could benefit a large amount of clinical diagnoses.

1.2 Goal

The goal of this project is to improve the B_0 uniformity in the neck using pyrolytic graphite. We aim for a numerical algorithm that provides us with an experimentally applicable design for a pyrolytic graphite composite foam that could efficiently homogenize the B_0 field in any given ROI. We study the B_0 passive shimming approach of covering the skin with a susceptibility-matching material from both an experimental and a mathematical viewpoint.

In the experimental study, our goal is to create a device that homogenizes the B_0 field in the region of the neck. We follow the procedure presented in the article of Lee $et\ al.\ [6]$. The material used is a pyrolytic graphite (PG) composite foam. PG microparticles are uniformly and randomly dispersed into a polyurethane foam. By determining the volume fraction of PG microparticles inside the foam, we want to create a bulk isotropic material with a specific magnetic susceptibility for passive shimming of the B_0 field inhomogeneities. Other studies used a bag of pineapple juice in order to homogenize the B_0 field in the area of the brachial plexus [7]. However, this fluid bag is usually very heavy and therefore, uncomfortable for the patient. In contrast, we use a lightweight and simple to shape PG foam. The PG foam is a good alternative to the fluid-matching agents as it is comfortable for the patient and it can be embedded directly within a radio frequency (RF) coil [6]. Furthermore, it is non-conductive and it does not produce MRI signal [6]. As PG foams can more easily be shaped than the other passive shimming approaches using bags of fluids, they allow for more complex designs.

Parallel to the experiments, we aim to investigate this shimming approach from a more mathematical and computational viewpoint as opposed to the experimental studies which already exist in the literature [6–8]. We wish to create a numerical algorithm for the design of a shim that homogenizes the B_0 field in a desired ROI. The algorithm should provide us with a magnetic susceptibility distribution for a neck shim, which generates a magnetic field that compensates for the field inhomogeneities in the ROI caused by the body.

1.3 Thesis Outline

The outline of this thesis is as follows:

Chapter 2: Preliminaries

First, we introduce some of the basic principles of MRI including the main static magnetic field B_0 . Then, we explain the origin of B_0 field inhomogeneities and we focus on the passive shimming technique as a tool for eliminating these field disturbances. We finish this chapter by briefly explaining B_0 field mapping techniques.

Chapter 3: PG Foam for B_0 Passive Shimming: an Experimental Study

In this chapter, we study the tissue susceptibility matched PG foam. First, we introduce the PG and the properties of the PG composite foam. We present the formula of the magnetic susceptibility of the PG foam as a function of the volume fraction of the PG particles and the bare foam (the foam without any PG). Then, we describe the PG foam construction, and the phantom used to observe and quantify field gradients near different susceptibility interfaces. Next, we experimentally investigate the dependence of the magnetic susceptibility of the PG foam on the volume fraction of PG microparticles. Finally, we show the $in\ vivo\ B_0$ field maps using a PG foam that we built for the neck. We compare the experimental field with simulations.

Chapter 4: Optimum PG Foam Design: a Numerical Study

This chapter covers the main mathematical and computational steps taken to attain an optimum design of PG foam capable of homogenizing the B_0 field perturbations generated near the skin. We show the numerical results by using two type of algorithms to solve the problem: a gradient descent algorithm and an improved version of it, a level set optimization integrated into a gradient descent framework.

Chapter 5: Conclusion

Chapter 5 completes this thesis by giving a summary and outlining the conclusions of this project.

Chapter 2

Preliminaries

In this chapter, we give a brief introduction to the MRI physics, B_0 shimming and B_0 field mapping. For a more comprehensive survey on MRI physics, imaging and hardware, the reader may refer to [9].

2.1 Basic Principles of MRI

In this section the basic phenomena involved in MRI are explained. For a detailed study of the physics behind the magnetic resonance, the reader should refer to the following books: [9–11]. MRI is a medical imaging technique used in radiology to non-invasively visualize internal structures of the human body and physiological processes. MRI is based on the physical phenomenon of nuclear magnetic resonance (NMR) to generate images of certain nuclei in the body. Atoms with an odd total number of protons and/or neutrons in their nuclei possess a fundamental quantum mechanical property known as spin. Hydrogen (1 H), carbon (13 C), sodium (23 N_a), and phosphorous (31 P) are some examples of these type of atoms. We study the case of a proton as it is the simplest one.

Spin is an intrinsic form of angular momentum (P) and it can be viewed as the proton spinning around an internal axis of rotation. This rotation results in a magnetic moment (μ) because the proton is charged. In quantum mechanics, angular momentum is quantized, meaning that it cannot vary continuously, but only between certain allowed values [12]:

$$\left| \vec{P} \right| = \frac{h}{2\pi} [I(I+1)]^{1/2}$$
 (2.1)

where h is the Planck's constant and I is the spin quantum number. For this analysis, we consider I to be $\frac{1}{2}$ as it corresponds to atoms such as ${}^{1}H$, ${}^{13}C$ and ${}^{31}P$.

The magnitude of the magnetic moment is given by [9]:

$$|\vec{\mu}| = \gamma \left| \vec{P} \right| = \frac{\gamma h \sqrt{3}}{4\pi},\tag{2.2}$$

where γ is the nuclear gyromagnetic ratio [13].

The x, y and z components of μ can have any value that satisfy the above equation. However, when a magnetic field is applied in the z direction, the B_0 field, the z component of μ is quantized. In the case of a proton, for which the magnetic quantum number takes values $\pm \frac{1}{2}$, μ_z can have 2 different values [12]:

$$\mu_z = \pm \frac{\gamma h}{4\pi} \tag{2.3}$$

In the following figure two cases are represented. In the first case (fig. 2.1(a)) there is no B_0 field applied and the μ has random orientations. The nuclei occupy a single energy level. In the second case (fig.2.1(b)) there is a B_0 field and this leads to the creation of two energy levels (Zeeman spliting [14]) depending on whether the μ_z is aligned parallel or anti-parallel to the B_0 . The energy difference of the two energy levels in the presence of a magnetic field is:

$$\Delta E = B_0 \left[\frac{\gamma h}{4\pi} - \left(-\frac{\gamma h}{4\pi} \right) \right] = \frac{\gamma h B_0}{2\pi} \tag{2.4}$$

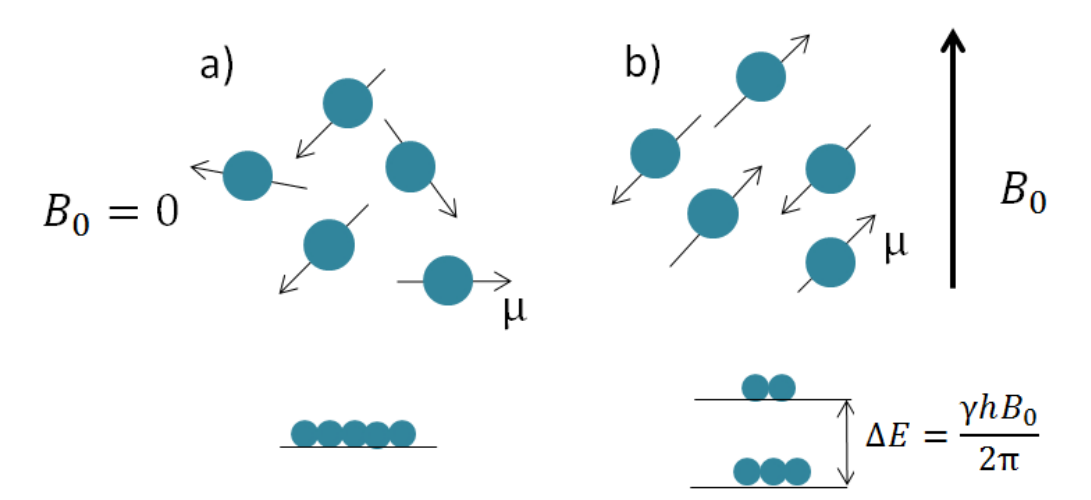


Fig. 2.1 (a) The μ -s of the protons are randomly orientated when there is no a magnetic field applied. The nuclei populate a single energy level. (b) In this case an external magnetic field is applied $(B_0 \neq 0)$ and the μ_z of the protons becomes quantized. μ_z can take two different orientations either in the direction of the B_0 or against it. These two orientations correspond to two different energy levels and the energy difference between them is ΔE . There are more nuclei in the lower energy level which corresponds to the orientation parallel to the B_0 .

The sum of all the net moments μ gives a net magnetization M_0 . M_0 is the maximum value of net magnetization at equilibrium along the direction of the main magnetic field (fig. 2.2(a)). Hence, M_0 is proportional to the difference in populations between the two energy levels [9]:

$$M_0 = \sum_{N=1}^{N_{\text{total}}} \mu_{z,n} = \frac{\gamma h}{4\pi} (N_{\text{parallel}} - N_{\text{anti-parallel}}), \tag{2.5}$$

where N_{total} is the total number of protons, i.e., $N_{total} = N_{parallel} + N_{anti-parallel}$. Using Boltzmann's and the first two terms of the Taylor series expansion of the exponent, the ratio of the number of protons in the two energy levels is given by:

$$\frac{N_{\rm anti-parallel}}{N_{\rm parallel}} = \exp\left(-\frac{\Delta E}{K_{\rm B}T}\right) \approx 1 - \frac{\Delta E}{K_{\rm B}T},\tag{2.6}$$

where $K_{\rm B}$ is the Boltzmann constant and T is the absolute temperature in degrees Kelvins.

In general, the exponent is extremely small and N_{parallel} and $N_{\text{anti-parallel}}$ are nearly the same and approximately half of the total number of nuclei. Therefore: $\Delta N = N_{\text{parallel}} - N_{\text{anti-parallel}} = \frac{N_{\text{parallel}}\Delta E}{K_{\text{B}}T} \approx \frac{N_{\text{total}}\Delta E}{2K_{\text{B}}T}$. And the M_0 is given by:

$$M_0 \propto \frac{\gamma^2 h^2 B_0 N_{\text{total}}}{K_{\text{B}} T} \tag{2.7}$$

The net magnetization is directly proportional to the B_0 field. As a consequence, strong B_0 fields are required for a bigger energy difference between the two levels and therefore, a bigger difference of populations which leads to a better MR signal.

In order to detect an MR signal, transitions between the two energy levels must occur. By applying an RF field orientated orthogonal to the B_0 field for a short duration, an RF pulse is created and energy is applied to the nuclear spin system. The pulse is applied at a specific resonance frequency (w_0) which is related to the ΔE of the system via:

$$\Delta E = \hbar \omega_0 \tag{2.8}$$

The ω_0 is known as the Larmor frequency and depends linearly on γ and B_0 : $w_0 = \gamma B_0$.

Classical mechanics predicts that the RF pulse, which is applied along one axis, produces a torque perpendicular to that axis (fig. 2.2(b)). M_0 is rotated by the *tip angle* α [9]. After applying the RF pulse with tip angle α about the x-axis, the magnetization along the x, y and z directions is:

$$M_{\rm x} = 0, M_{\rm y} = M_0 \sin \alpha, M_{\rm z} = M_0 \cos \alpha \tag{2.9}$$

When the RF pulse is turned off, the transverse component of the magnetization (M_{xy}) precesses around the B_0 axis at the Larmor frequency (fig.2.2(c)). It should be noted that the exact precession frequencies of different nuclei within a molecule depend also on the chemical shift and scalar coupling. For information about these topics, the reader may refer to the reference [9].

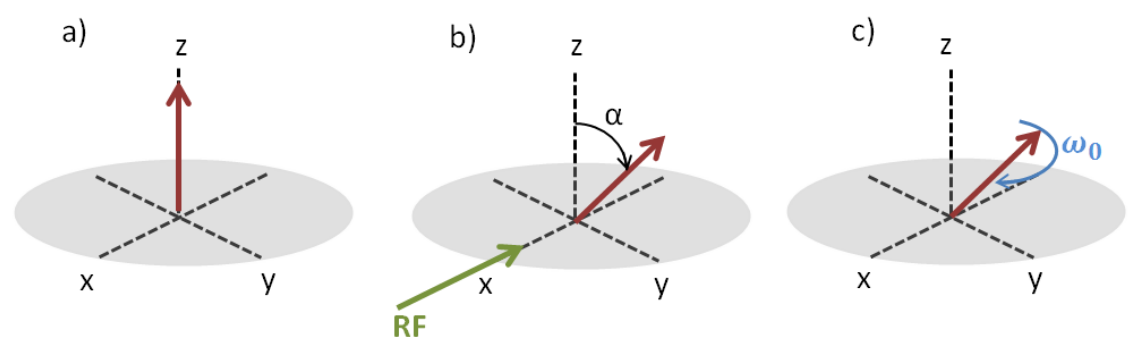


Fig. 2.2 (a) After applying a external magnetic field B_0 the nuclei of the protons align with the B_0 giving a net magnetization M_0 . (b) An RF pulse is applied along the x axis. The magnetization rotates by an angle α about the x axis. (c) Immediately after the RF pulse, the magnetization starts to precess at a frequency. This frequency is the same as the frequency of radiation ω_0 .

Nevertheless, the magnetization components do not stay in those conditions forever, they will return to their thermal equilibrium values: $M_y = 0, M_x = 0, M_z = M_0$. The time-evolutions of M_z , M_y and M_x are given by the Bloch equations [15]:

$$\frac{dM_{x}}{dt} = \gamma M_{y} \left(B_{0} - \frac{w}{\gamma} - \frac{M_{x}}{T_{2}}\right)$$

$$\frac{dM_{y}}{dt} = \gamma M_{z} B_{1} - \gamma M_{x} \left(B_{0} - \frac{w}{\gamma} - \frac{M_{y}}{T_{2}}\right)$$

$$\frac{dM_{z}}{dt} = -\gamma M_{y} B_{1} - \frac{M_{z} - M_{0}}{T_{1}}$$
(2.10)

 T_1 is the spin-lattice relaxation time and it governs the return of M_z to its equilibrium value. At the same time, T_2 is the spin-spin relaxation time and it governs the return of the components M_x and M_y . The values for the two relaxation times depend on the types of sample, but T_1 is always greater than T_2 .

In MRI experiments, a volume coil is typically used to transmit the RF pulses while multiple surface coils are typically used to receive the signal. The MR signal is measured via the inductive coupling between the magnetization vector and the receiver coils. While M_{xy} is precessing around B_0 with the Larmor frequency, a time-varying magnetic flux is induced in the coil which induces a measurable time-varying voltage. The strength of the received signal does not only depend on the T_1 and T_2 relaxation times, but also on the spin density (ρ_0) . ρ_0 is the number of protons per unit volume and M_0 is directly proportional to it.

In order to have information about the spatial position of the received MR signals, magnetic field gradient coils are necessary. The gradient coils are conductors through which current passes. This results on the generation of a gradient field, which produces a linear dependence of the magnetic field on spatial location.

Particular combinations and timings of RF pulses, gradient field waveforms and signal acquisitions are known as pulse sequences. In most pulse sequences there are two main parameters: the repetition time (TR) and the echo time (TE). TR is the interval time between corresponding consecutive points on a repeating series of pulses and echoes. The TE is the time between the RF pulse and echo time, which refocuses the spin magnetization.

2.2 B_0 Shimming

One of the biggest challenges in MRI technology is to obtain a homogeneous main magnetic field B_0 . The spatial uniformity of the B_0 is crucial for most of the MR applications. The presence of inhomogeneities in this magnetic field can lead to a large number of artifacts such as image distortions, intravoxel dephasing, blurring and non-accurate fat suppression. Furthermore, the B_0 inhomogeneities are directly proportional to the magnitude of the applied magnetic field B_0 , which results on high perturbations at 3T or above. For some clinical applications, artifact-free imaging at 3T and above may become very difficult. The majority of the field perturbations are sample-induced, i.e., the difference in magnetic susceptibility between materials or tissues leads to a disturbance in the magnetic field.

Applying a homogeneous magnetic field B_0 to a continuous material, the total magnetic field (B_{total}) inside the material is given by [9]:

$$B_{total} = B_0 + \mu_0 M, \tag{2.11}$$

where M is the magnetization induced inside the material: $M = (\chi/\mu_0)B_0$. In this expression χ is the magnetic susceptibility of the material and μ is the magnetic permeability. They are related according to $\chi = (\mu/\mu_0) - 1$, where μ_0 is the vacuum permeability. χ is dimensionless and describes how μ deviates from μ_0 . Magnetic susceptibility is a property of every material and indicates the degree of magnetization of a material in response to an applied magnetic field. If χ is negative, the material is classified as diamagnetic and the magnetization inside the material opposes the applied field B_0 . This results in a net reduction of the B_0 . Examples of diamagnets are water and soft tissues. If χ is positive, the material is classified as paramagnetic and the magnetization inside the material strengthens the B_0 . A well known paramagnetic material is air. Both diamagnetic and paramagnetic materials loose their magnetization when the external magnetic field is removed. Ferromagnets, which have a large and positive χ , retain their magnetization and they are usually incompatible with MRI experiments. In table 1, we show a list of the different magnetic susceptibilities of the most important anatomical tissues.

ference
Terence
[16] [17] [17] [17] [17] [17]
[17] [18]

Table 1 Magnetic susceptibility values of anatomical tissue types.

In the following figure the susceptibility distribution of the coronal axis of the upper part of the human body is shown (fig. 2.3a); and also, the magnetic field induced by that susceptibility distribution (fig. 2.3b). The human body model used for these simulations, and also throughout this thesis, is DUKE [19].

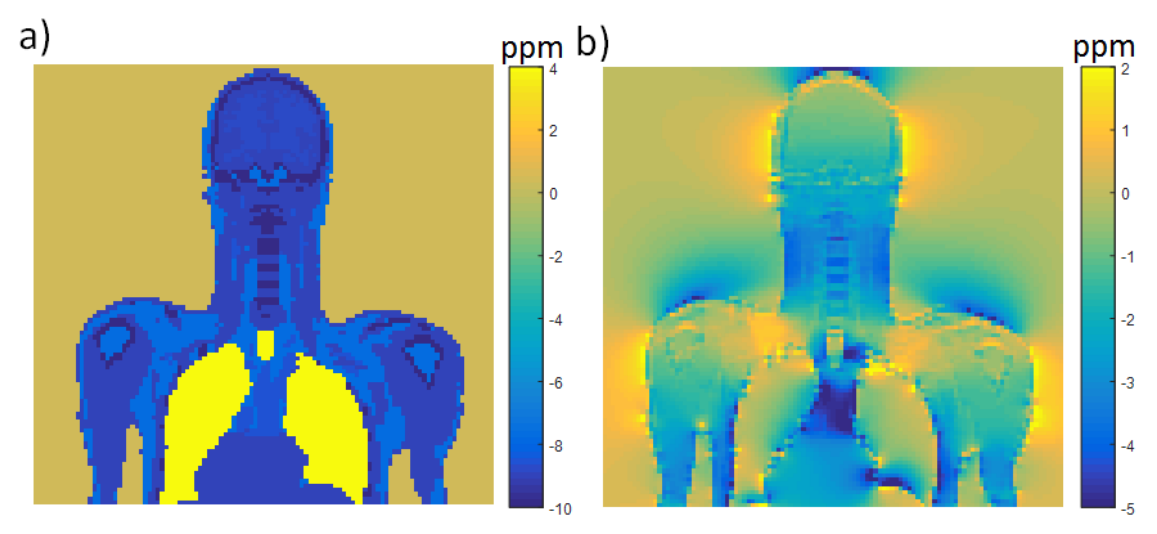


Fig. 2.3 (a) Magnetic susceptibility of the human body model. (b) Magnetic field induced by the magnetic susceptibility distribution in a. The B_0 offset ranges between -2 ppm and 2 ppm.

Magnetic field inhomogeneities are created due to the differences in magnetic susceptibilities in the human body (table 1). Mostly air-tissue interfaces generate high spatial frequency perturbations. The change in induced magnetization is given by:

$$\Delta M = \left(\frac{\chi_{\text{tissue}} - \chi_{\text{air}}}{\mu_0}\right) B_0 \tag{2.12}$$

The change in magnetization leads to a magnetic field distribution $(\Delta B(\vec{r}))$. The B_0 inhomogeneity induced by a magnetic susceptibility distribution in space, $(\chi(\vec{r'}))$, is given

by [22]:

$$\Delta B(\vec{r}) = B_0 \int_{r' \in v'} G(\vec{r} - \vec{r'}) \cdot \chi_{(\vec{r'})} d\vec{r'}, \qquad (2.13)$$

where r' denotes the position vector in the region of varying susceptibility, v', and r denotes the position vector in the region within to evaluate the $\Delta B(\vec{r})$. G is the Green's function of the system, i.e., it relates the $\chi(\vec{r'})$, to the induced field perturbations $\Delta B(\vec{r})$ (see figure 2.4).

The most common approach to solve this direct problem is to apply the convolution theorem to equation 2.13, so that Fast Fourier Transforms (FFT) may be used. The use of FFT-s improves the computation speed and the quantities numerically convolved (G and χ) must have the same matrix size and consistent coordinate axes. Using FFT-s, the field homogeneities are given by the expression [20,21]:

$$\Delta B(\vec{r}) = B_0 \cdot F T^{-1} \left[F T(G(\vec{r})) \cdot F T(\Delta \chi(\vec{r})) \right],$$
where,
$$G(\vec{r}) = \frac{1}{4\pi} \frac{2z^2 - x^2 - y^2}{(x^2 + y^2 + z^2)^{5/2}}$$
(2.14)

 $G(\vec{r})$ is the Green's function of the system in the spatial domain and FT and FT^{-1} are the forward and inverse Fourier Transformations (FT). And $\Delta\chi(\vec{r}) = \chi_{\rm tissue} - \chi_{\rm air}$. After computing the FT of $G(\vec{r})$, the equation can be rewritten as [20]:

$$\Delta B(\vec{r}) = B_0 \cdot FT^{-1} \left[\left(\frac{1}{3} - \frac{k_z^2}{k^2} \right) \cdot FT(\Delta \chi(\vec{r})) \right], \tag{2.15}$$

where k is the coordinate in reciprocal k-space and $k^2 = k_x^2 + k_y^2 + k_z^2$. Not only the amplitude of the magnetic susceptibility, but also its spatial distribution (*i.e.* the geometry of the body) strongly affects the field inhomogeneity.

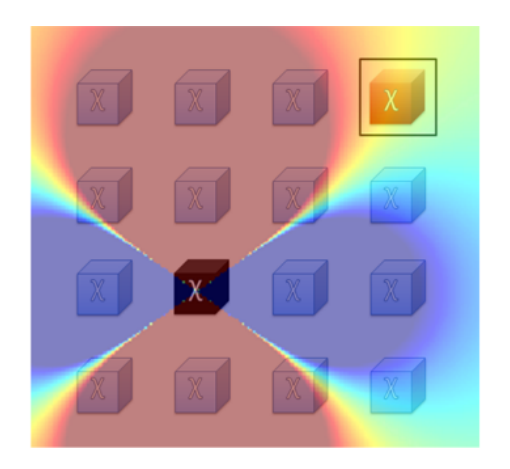


Fig. 2.4 Figure taken from reference [22]. A source susceptibility region (black) and a target region (red with black outline). The spatial Green's function originates from a source susceptibility region and it overlaps a target region.

 B_0 shimming is the process by which the main magnetic field is made more homogeneous. The non-uniformity of the B_0 field can be reduced with either passive or active methods. In active shimming, currents are directed through specialized coils to further improve homogeneity. In passive shimming, however, a magnetic material is placed at strategic locations in order to compensate the B_0 within an adjacent ROI. A very commonly used active shimming approach to minimize magnetic field variations is to superimpose secondary magnetic fields with a spatial variation governed by spherical harmonic (SH) functions [9]. Nevertheless, the static spherical harmonic shimming applications do not usually go above the 3^{rd} order of correction [23–25]. Hence, the high spatial frequency field perturbations in some regions of the body cannot be corrected with this shimming method. A method to correct these uniformities could be to cover the skin with a tissue susceptibility-matched material to move the inhomogeneities outside the ROI. This is a simple and passive technique and its good performance has been proven previously with several different materials. Most of the versions of this technique include bags of fluid, such as perfluorocarbon [26], barium sulfate-doped water [27] or pineapple juice [7]. In 2010, Lee et al presented a passive method to improve the B_0 uniformity near the skin using PG [6]. By uniformly dispersing PG microparticles in a closed-cell foam, they experimentally create a PG foam with the same magnetic susceptibility of water, which is $\chi_{\text{water}} = -9 \times 10^{-6} = -9 \text{ ppm}.$

2.3 B_0 field mapping

The characterization of the magnetic field inhomogeneity is a process known as B_0 mapping. The B_0 field perturbations are usually obtained from the phase difference of two images acquired at two different echo times during a period of free precession, which yields:

$$\Delta \phi = \phi_2 - \phi_1 = \omega (TE_2 - TE_1), \tag{2.16}$$

where $\phi_1 = \phi_0 + \omega T E_1$ and $\phi_2 = \phi_0 + \omega T E_2$. ϕ_0 is the initial phase given by the RF excitation. ω is related to the local B_0 inhomogeneities and it is given by: $\omega = \gamma \Delta B_0$, where γ is the gyromagnetic ratio of the proton.

The B_0 field variation is given by:

$$\Delta B_0 = \frac{\Delta \phi}{\gamma \Delta T E},\tag{2.17}$$

where $\Delta TE = TE_2 - TE_1$.

Chapter 3

PG Foam for B_0 Passive Shimming: an Experimental Study

In MR studies, image signal and contrast is highly dependent on the uniformity of the B_0 static field. The B_0 field becomes inhomogeneous due to the difference in magnetic susceptibilities between materials and tissues; in particular, the 9 ppm susceptibility difference between air and tissue produces strong perturbations. In this chapter, we study the PG composite foam as a B_0 passive shimming approach to reduce the non-uniformities in the B_0 main field. The advantages of the PG foam is that it is lightweight, simple to shape and can be embedded directly within an RF coil [6]. Comparing with other susceptibility matching materials, such as fluid bags, PG foam may be more comfortable for the patient as it can be shaped to conform the body and it is less heavy. Also, it is non-conductive and it does not produce MRI signal [6]. First, we introduce the properties of the PG foam and the formula for its magnetic susceptibility. Next, we explain the materials and methods used for our experiments. Finally, we present the results, which experimentally demonstrate that the PG foam compensates for the inhomogeneities generated by the airwater interface and it improves the inhomogeneities of the static field in the region of the neck.

3.1 Pyrolytic Graphite foam as a magnetic susceptibility matching material

Pyrolytic graphite or pyrolytic carbon is a polycristalline form of carbon that has a hexagonal crystal structure and is similar to graphite. PG is an artificial material, it is not found in nature [28]. It is generally produced by heating a hydrocarbon nearly to its decomposition temperature, and permitting the graphite to crystallize. This crystallization occurs in a planar order producing a single cleavage plane. This leads to the unusual characteristic of PG: it posses anisotropic properties [29]. It is more electrically conductive parallel to its crystal plane than perpendicular to the plane: up to 10⁴ times more [30]. It is also one of the best planar thermal conductors available. However, what makes PG a

powerful tool for B_0 passive shimming is that it exhibits the highest diamagnetism of any room-temperature diamagnet. This high χ is only presented in the plane orientated perpendicular to the crystal plane ($\chi_{\perp} = -595$ ppm) [31]. PG's anisotropic magnetic susceptibility exhibits 70 times greater χ in the perpendicular orientation rather than the parallel orientation ($\chi_{\parallel} = -8.5$ ppm) [31].

3.1.1 Magnetic Susceptibility of PG foam

Powdered PG particles are embedded into a closed-cell polyurethane foam. The average susceptibility of the PG foam is given by [6,31]:

$$\chi_{\text{average}} = \frac{f\chi}{1 + \alpha\chi},\tag{3.1}$$

where f is the volume fraction of the PG particles, χ is the overall magnetic susceptibility of the particles and α is a shape dependent factor [31].

The value of χ is of the order of 10^{-6} , therefore the above equation can be simplified to:

$$\chi_{\text{average}} \approx f \chi$$
 (3.2)

In our case, the magnetic susceptibility of the PG foam (χ_{PGf}) is a three component mixture of: PG particles, bare foam and air. It is given by:

$$\chi_{\text{PGf}} = \chi_{\text{PG}} \cdot f_{\text{PG}} + \chi_{\text{f}} \cdot f_{\text{f}} + \chi_{\text{air}} \cdot f_{\text{air}}, \tag{3.3}$$

where χ_{PG} is the magnetic susceptibility of randomly dispersed PG particles with a volume fraction f_{PG} . χ_f is the magnetic susceptibility of the foam when there is no particles inside and it takes takes the volume fraction f_f . Air is the third component of the mixture and it will take the volume fraction $f_{air} = 1 - f_{PG} - f_f$, because the sum of all the volume fractions gives 1.

 $\chi_{\rm PG}$ is the average of the directional components of the magnetic susceptibility of PG:

$$\chi_{\rm PG} = \frac{\chi_{\rm x} + \chi_{\rm y} + \chi_{\rm z}}{3} = \frac{\chi_{\perp} + 2\chi_{\parallel}}{3} = \frac{-595 + (2 \times (-8.5))}{3} [\rm ppm] = -204 [\rm ppm]$$
(3.4)

The magnetic susceptibility of the bare foam (without any PG particles) can be estimated from literature. Wapler et~al. published in 2014 the magnetic susceptibilities of a large number of polyurethane foams. They found that all the polyurethane foams they studied have a susceptibility close to the one of water ($\chi_{\text{water}} = -9 \text{ ppm}$) [32]. This statement opposes Lee et~al. articles ([6,8]) in which they claim that their polyurethane foams have a χ close to the one of air ($\chi_{\text{air}} = 0.36 \text{ ppm}$). By relying on Wapler et~al. results for the χ_f , we conclude that the theoretical value of the magnetic susceptibility of the PG foam depends on the volume fraction of the PG particles and on the volume fraction of the bare foam in the following way:

$$\chi_{\text{PGf}} = -204.4 f_{\text{PG}} - 9.4 f_{\text{f}} + 0.36 [\text{ppm}],$$
(3.5)

where we consider that $\chi_{air} = 0.36$ ppm.

Consequently, by determining the volume fraction f_{PG} of PG particles and the one of the bare foam f_f , we can obtain a PG foam with a desired magnetic susceptibility.

3.1.2 Electrical Conductivity of the PG foam

It is very important that the material used for MRI applications is non-conductive. Under a radio frequency magnetic field, conductive materials generate eddy currents creating thermal heat. This could be harmful for the patient and must always be avoided. Moreover, the electrical conductivity of the PG foam can also lead to noise in our signal, as the noise scales linearly with the conductivity [33].

In order to study the electrical conductivity of the PG foam, the effective Medium Theory (EMT) is used. EMTs are used to describe the macroscopic properties of composite materials [34,35]. To predict the conductivity of the effective media ($\sigma_{\rm em}$) the EMTs utilize the symmetric media Bruggeman equation for spherical inclusions of high conductivity in a low conductivity matrix [6,36]:

$$f_{1}\frac{\sigma_{1} - \sigma_{\text{em}}}{\sigma_{1} + 2\sigma_{\text{em}}} + f_{h}\frac{\sigma_{h} - \sigma_{\text{em}}}{\sigma_{h} + 2\sigma_{\text{em}}} = 0,$$
(3.6)

where f_h is the volume fraction of the highly conducting component with conductivity σ_h and f_l is the volume fraction of the insulating component with conductivity σ_l .

In our case, the highly conducting component is the PG particles and the insulating component is the bare foam. The PG has a very high conductivity in plane ($\sigma_{PG} = 1.9 \times 10^6 \text{ S/m}$) [6,30]. The conductivity of the bare foam, however, is $\sigma_f = 10^{-4} \text{ S/m}$ [37]. For safety reasons, the conductivity of the PG foam should be two orders of magnitude below that of human tissue, which is in the order of 1 S/m. Equation 3.6 shows that the PG foam is MRI compatible until the volume fraction of PG particles is ≈ 0.16 , i.e. the electrical conductivity of the foam should ideally be below 5 mS/m (two orders of magnitude below the σ of the human tissue), and we obtain that value when the volume fraction of the PG particles is approximately 16% [6,38].

Also, we must avoid the PG foam to add significant amount of noise to the MRI scan. In section 3.3.1, we study the signal-to-noise ratio and the effect of the PG foam on it.

3.2 Materials and Methods

We present the materials and the methodology to construct the PG foam and to subsequently characterize it. All MR experiments are performed in a 3T Philips MR scanner.

3.2.1 PG foam construction

For creating a PG foam foam, we use high purity PG powder and two-component polyurethane polymer foam. The PG powder is manufactured by Graphite Machining, Inc., Topton, Pennsylvania. The diameter of the particles is 44 μ m. The polyurethane foam is purchased from Smooth-On, Inc., Amsterdam, The Netherlands. The product name is FlexFoamit(6), which expands 10 times its original volume. Our goal is to obtain a PG foam with a randomized, uniform dispersion of PG microparticles throughout the entire foam. First, we mix the PG powder and one component of the foam. We throughly mix them so that the PG powder is uniformly dispersed. Next, we pour the second component to the mixture. We again make sure the mix is as homogeneous as possible so that the PG microparticles are uniformly distributed. Before the foam expands, the foam is poured in plastic containers or custom built plastic molds. Finally we allow it to rise and cure. The magnetic susceptibility of the final PG foam depends on the amount of PG powder in the foam. The volume fraction of the PG powder that we use in our mixture is inversely proportional to the volume where we let the foam expand. The amount of bare foam used does not play a mayor role when constructing the foam. The reason for this is that the magnetic susceptibility of the PG (-204 ppm) is much more negative than the one of the bare foam (-9 ppm), therefore, relatively small changes in the volume fraction of the bare foam do not significantly change the final magnetic susceptibility of the PG foam. Nevertheless, we want to underline that even if the density of the bare foam does not dramatically change the outcome, it does have an effect.



Fig. 3.1 PG powder. The diameter of the particles is 44 μ m.

3.2.2 SNR

In order to test whether the PG foam has an effect on the Signal-to-Noise Ratio (SNR), we used a cylinder filled with doped water as an SNR phantom. Gradient echo images were acquired both with a regular foam as well as a PG foam below the cylinder. The foams have a thickness of 2 cm. The FOV is 18×26 cm² and the slice thickness is 2.8 mm. Repetition time and echo time are: TR = 6 ms and TE = 2.6 ms, respectively. $\Delta TE = 0.8$ ms. The formula of the SNR is the following:

$$SNR = \frac{S}{\sigma_{\rm N}},\tag{3.7}$$

where S is the signal amplitude and σ_N is the standard deviation of the background noise. We compare a PG foam with a volume fraction of 4% of PG powder, i.e., with a magnetic susceptibility of -9 ppm, and a regular foam with no PG powder, i.e., with a magnetic susceptibility of roughly zero (after expansion).

3.2.3 Phantom

A phantom was constructed to measure the B_0 field inhomogeneity near different susceptibility interfaces. The phantom has the shape of a hollow cylinder, with an external radius, R, and an internal radius, r. The outer cylinder is filled with regular water. Inside the inner cylinder we place a cylindrical plastic tube, which we fill with either water, air or different PG foams (fig.3.2). The plastic tubes have a total volume of 58 ml.

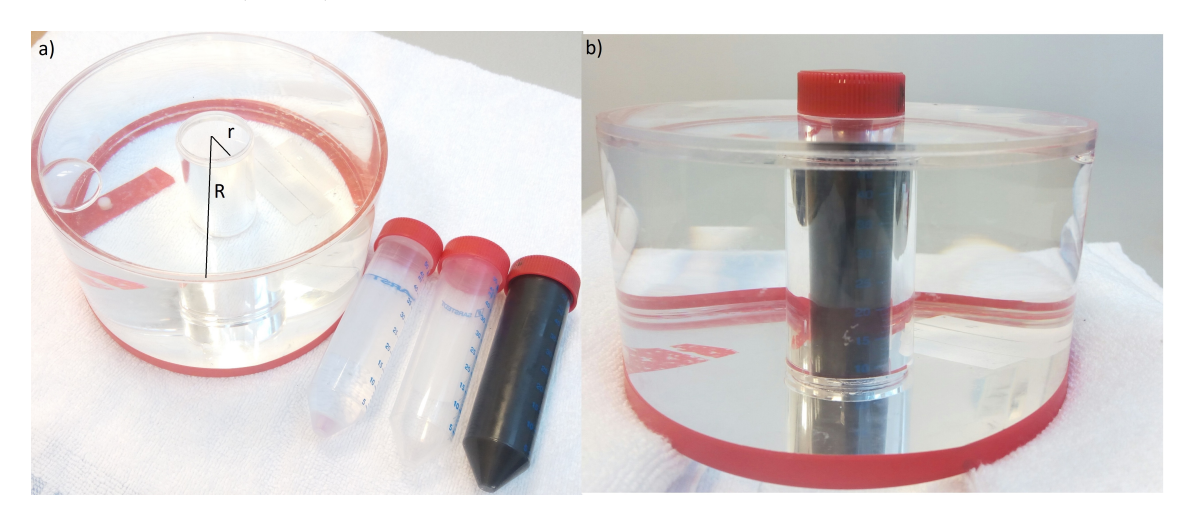


Fig. 3.2 (a) The phantom has a shape of a hollow cylinder with an inner radius of r = 1.5 cm, and an external radius of R = 7.5 cm. The plastic tubes next to the phantom are filled with water, air and PG foam (left to right). (b) Tube filled with PG foam placed in the phantom.

We acquire B_0 maps of the phantom. The phantom is oriented orthogonal to the static B_0 field. We acquire 2D gradient echo images with a FOV of 16×16 cm² and a 20 mm slice thickness. The repetition time is 10 ms and the echo time is 2.2 ms. The difference between the echo times is $\Delta TE = 0.8$ ms.

3.2.4 PG foam neck shim

We construct a 2 cm thick sheet of PG foam (fig. 3.3a). We conform this sheet such that it covers the neck (fig. 3.3b).

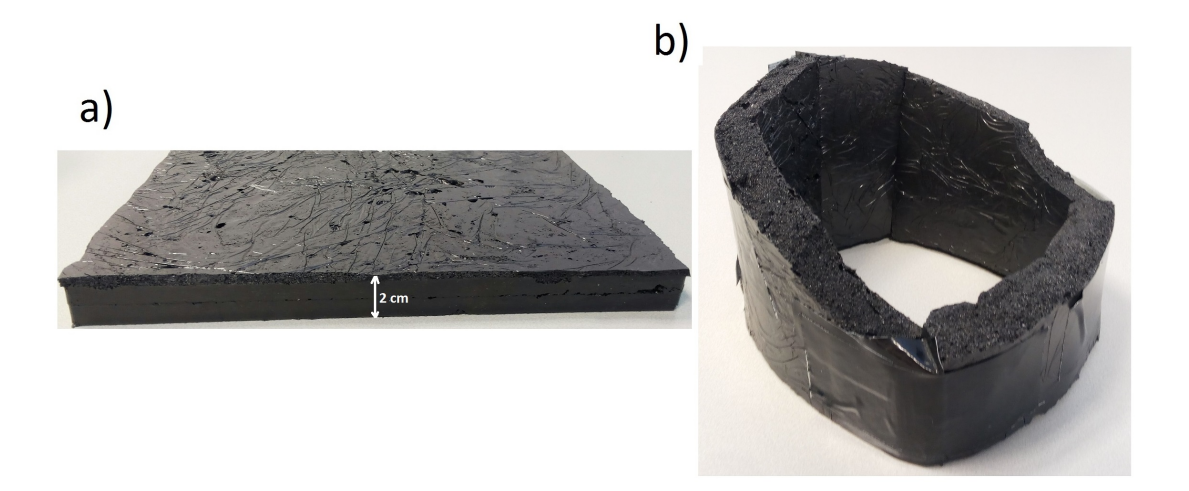


Fig. 3.3 PG foams with 4% volume fraction of PG microparticles, generating a PG composite foam with -9 ppm magnetic susceptibility. (a) 2cm thick sheet of PG foam. (b) PG foam neck shim, which can be placed around the neck in order to homogenize the B_0 field near the skin.

To test the PG foam neck shim, a healthy internal volunteer was recruited for the experiment. Sagittal 2D gradient echo images of the neck are acquired with and without a PG foam neck shim. The FOV is 32×48 cm² and the slice thickness is 2 cm. The repetition time is 10 ms and the echo time is 1.23 ms. $\Delta TE = 0.8$ ms.

3.3 Results and Discussion

In this section we present the experimental results. We begin by proving that the PG foam does not add any noise to the signal. Next, we characterize the PG foam in a phantom. We analyze B_0 field maps for different concentrations of PG in a fixed volume. Finally, we show *in vivo* field maps when using a PG foam neck shim and we compare them with the simulations.

3.3.1 SNR

In figure 3.4, we analyze the SNR values of each pixel along a line of the image. The SNR in every point is taken following equation 3.7. The SNR for the phantom with the PG foam and with the regular foam are virtually identical. Hence, we guarantee that the PG foam does not add any noise to the system.

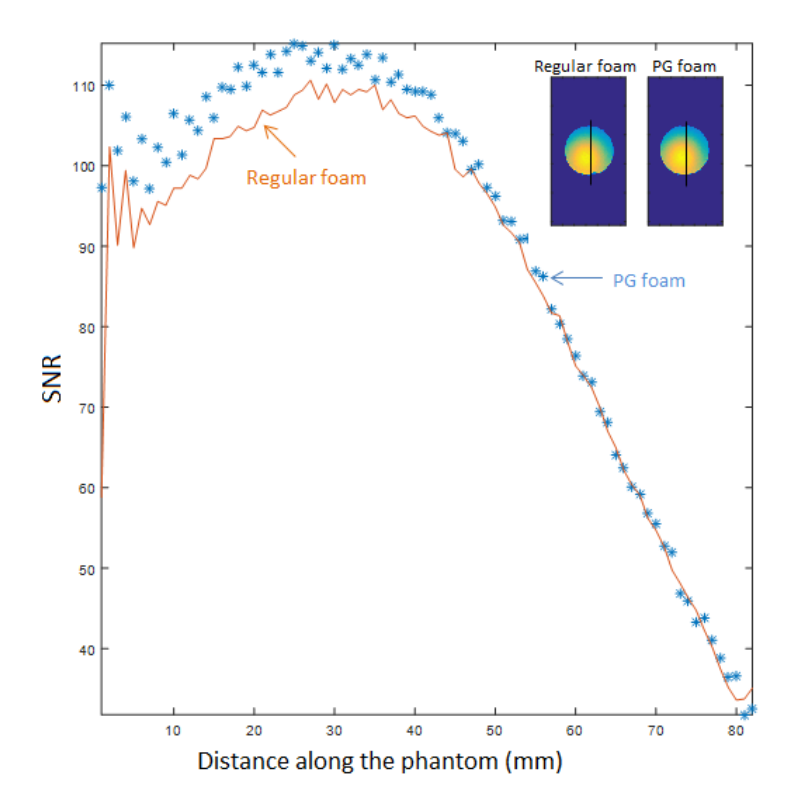


Fig. 3.4 SNR value along the phantom with a regular foam (orange) and with a PG foam (blue stars). The black line in the two figures of the inset represents the slice along which the SNR profiles are plotted. Figure on the left represents the SNR map of the phantom with the regular foam and the image of the left of the one with the PG foam.

In figure 3.4, we evaluate the pixel-wise SNR. Now, we take the average over the 2D slice, thus obtaining the total SNR, given by $\frac{\overline{S}}{\sigma_{\rm N}}$, where \overline{S} is the mean of the signal. We obtain a total SNR of 176 for the phantom with the PG foam and a total SNR of 175 for the phantom with a regular foam. The values are almost exactly the same.

Similar observations were made in a PG foam with a 7% of volume fraction of PG powder. With this percentage of PG powder, we expect a magnetic susceptibility around -17 ppm. In this case, we obtain a total SNR of 126 for the phantom with the PG foam and total SNR of 125 for the phantom with the regular foam. When plotting the pixel-wise SNR along the phantom, the SNR of the PG foam corresponds well to the SNR of the regular foam, showing the same behavior as the previous experiment (fig. 3.4). Hence, we have demonstrated that the SNR is not reduced when using PG foams with a

PG volume fraction up to 7%.

3.3.2 PG foam characterization

In this section we characterize the PG foam. We study foams with different concentrations of PG microparticles. We acquire the B_0 field maps using the phantom with the small cylinder filled with water, air and different PG foams. 3T coronal field maps are shown in figure 3.5. When the small cylinder of the phantom is filled with air (fig. 3.5(a)), the air-water interface causes the classical dipole pattern [58]. This pattern alternates positive and negative regions of B_0 field perturbations and it is created by a cylinder orientated perpendicular to the main magnetic field. When the inner cylinder of the phantom is filled with water, the B_0 field is constant, i.e., a perfect susceptibility matching is shown (fig. 3.5(b)). Figures 3.5(c), 3.5(d), 3.5(e), 3.5(f), 3.5(g) and 3.5(h) show the B_0 field maps generated when the volume fraction of PG in the foam is 0%, 1%, 2%, 3%, 4% and 5%, respectively. Note that the amount of bare foam is the same in all the cases so that the change in magnetic susceptibility only arises from the volume fraction of the PG.

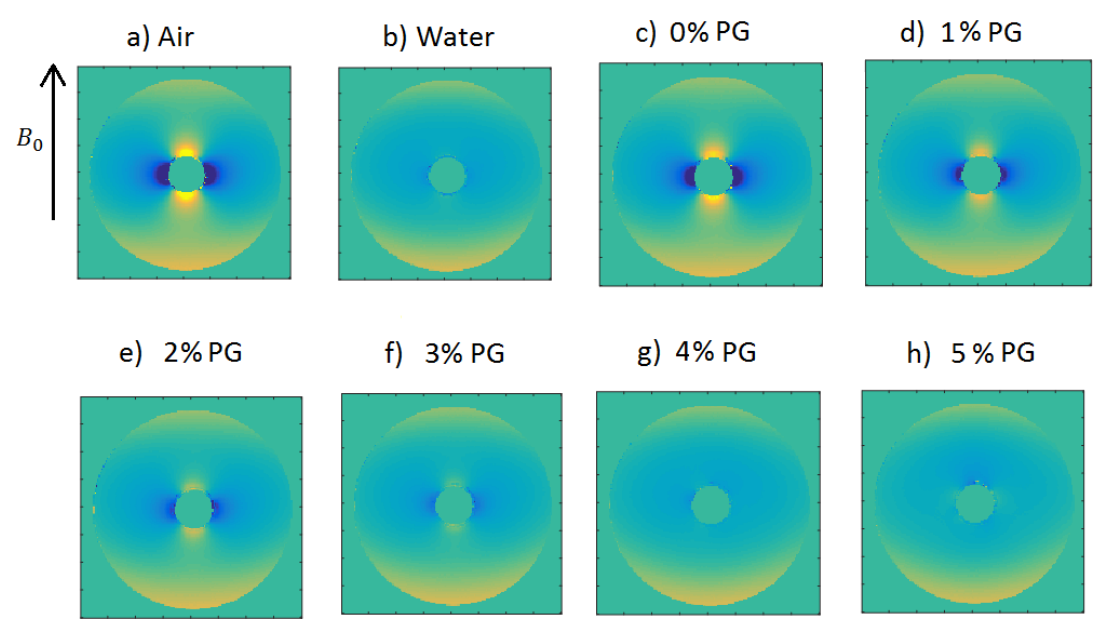


Fig. 3.5 B_0 field maps acquired in a 3T MRI scanner using a gradient echo sequence. TR = 10 ms, TE = 2.2 ms, slice thickness= 20 mm, FOV = 22.4×22.4 cm², matrix = 256×256 . ΔTE is 0.8 ms. Note that in all the cases, there are inhomogeneities arising around the outer interface of the phantom due to the air-water interface. (a) When the inner cylinder of the phantom is filled with air, a dipole effect is created. The difference of magnetic susceptibility of air and water generates perturbations in the B_0 field. (b) With water, however, the B_0 field is very homogeneous throughout the phantom (except in the outer interface, because there is air outside the phantom). (c) With bare foam, i.e., without any PG particles, the B_0 field is still very inhomogeneous. (d)-(h) Foams with different concentration of PG particles. We can see that as we increase the volume fraction of PG powder, the B_0 becomes more homogeneous.

We demonstrate that when the volume fraction of PG is 4% (fig. 3.5g), the PG foam demonstrates good susceptibility matching to water, thus creating the same pattern as in figure 3.5b. This implies that a foam with a 4% of volume fraction of PG powder presents the same magnetic susceptibility of the one of water: -9 ppm.

Next, we want to obtain the value of the magnetic susceptibility of each PG foam from the MR data. For this, we need to calculate the B_0 field inhomogeneities generated by only the PG foam. Hence, we need to get rid off any perturbations generated by the air or water.

$$B_{0,PGf'} = \frac{B_{0,PGf}}{B_{0,air}}$$

$$B_{0,water'} = \frac{B_{0,water}}{B_{0,air}},$$
(3.8)

where $B_{0,\text{air}}$ is the data obtained by filling the inner cylinder of the phantom with air, $B_{0,\text{water}}$ with water and $B_{0,\text{PGf}}$ with PG foams. $B_{0,\text{PGf'}}$ is the B_0 inhomogeneities generated only by the PG foam inside the tube and $B_{0,\text{water'}}$ by only the water inside the tube.

Equation 2.13 shows the B_0 inhomogeneity induced by a magnetic susceptibility distribution in space. However, if the magnetic susceptibility is constant throughout the space, i.e., it is not position dependent, it can be moved outside the integral. In our case, the χ of the PG foam inside the tube is constant throughout the volume of the tube. Therefore, the B_0 field inhomogeneities generated by the PG foam and the water (inside the plastic tube) are given by:

$$B_{0,\text{PGf'}}(\vec{r}) = B_0 \int_{r' \in v'} G(\vec{r} - \vec{r'}) \cdot \chi_{\text{PGf}} d\vec{r'} = B_0 \cdot \chi_{\text{PGf}} \int_{r' \in v'} G(\vec{r} - \vec{r'}) d\vec{r'}$$

$$B_{0,\text{water'}}(\vec{r}) = B_0 \int_{r' \in v'} G(\vec{r} - \vec{r'}) \cdot \chi_{\text{water}} d\vec{r'} = B_0 \cdot \chi_{\text{water}} \int_{r' \in v'} G(\vec{r} - \vec{r'}) d\vec{r'},$$
(3.9)

where r' denotes the position vector in the region of varying susceptibility, i.e., the volume of the tube v', and r denotes the position vector in the region within to evaluate the field inhomogeneities. G is the Green's function of the system.

We want to solve these system of equations for the χ_{PGf} . By dividing $B_{0,PGf'}$ and $B_{0,water'}$, we eliminate the geometric factor given by the Green's function. Using the theoretical value of the magnetic susceptibility of water, -9 ppm, we can solve for the magnetic susceptibility of the PG foam:

$$\chi_{\rm PGf} = \overline{\left(\frac{B_{0,\rm PGf'}}{B_{0,\rm water'}}\right)} \times \chi_{\rm water} = \overline{r} \times -9 \,[\rm ppm],$$
(3.10)

where the line over the ratio between the $B_{0,PGf'}$ and the $B_{0,water'}$ represents the mean: $\frac{\overline{B_{0,PGf'}}}{\overline{B_{0,water'}}} = \overline{r} = \frac{1}{N} \sum_{i=1}^{N} \frac{B_{0,PGf'}^{i}}{\overline{B_{0,water'}}^{i}}$. N is the number of scalar observations in the data.

In this way we can obtain the value of the magnetic susceptibility of the PG foams from the experimental data. In the following figure we plot the magnetic susceptibility of the PG foam as a function of the volume fraction of the PG particles.

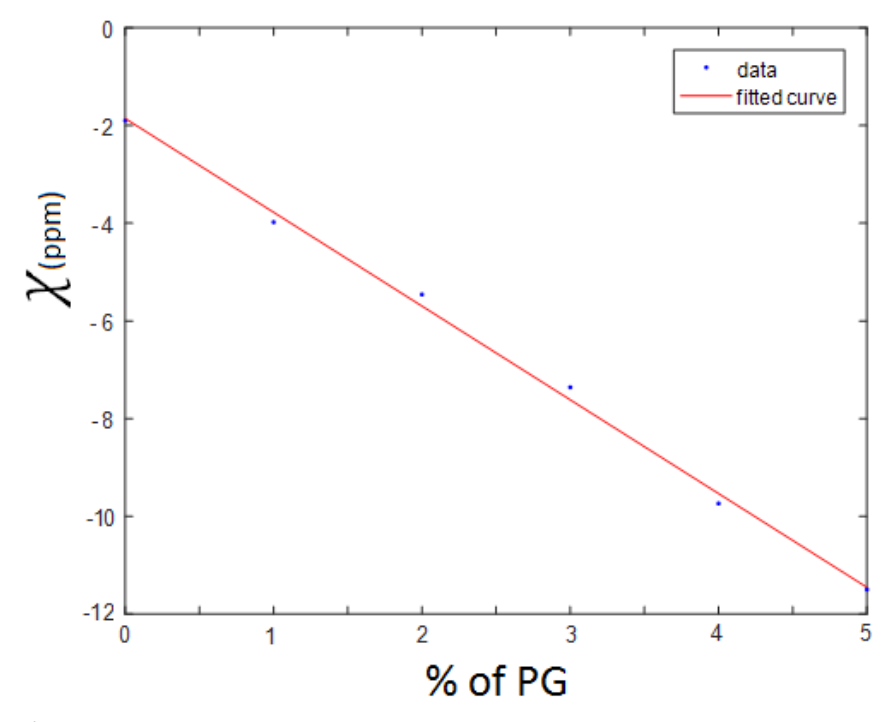


Fig. 3.6 Magnetic susceptibility of the PG foam versus the concentration of PG microparticles in the foam. The red line represents a linear fit to the data (blue dots).

The data is fitted to a first degree polynomial equation f(x) = ax + b, with a = -191.9 ppm and b = -1.86 ppm. We relate these values to the formula derived in section 3.1:

$$\chi_{\text{PGf}} = (\chi_{\text{PG}} - \chi_{\text{air}}) f_{\text{PG}} - (\chi_{\text{f}} - \chi_{\text{air}}) f_{\text{f}} + \chi_{\text{air}} [\text{ppm}]$$
(3.11)

From the experimental data, we find the value for the magnetic susceptibility of the PG and the value for the magnetic susceptibility of the bare foam to be:

$$\chi_{\text{PG}} = [-191.5 \pm 15.2] \text{ ppm}$$

$$\chi_{\text{f}} = [-8.9 \pm 1.9] \text{ ppm},$$
(3.12)

where we consider that $\chi_{\rm air}=0.36$ ppm. In this experiment, the volume fraction of the bare foam before it expands, $f_{\rm f}$, is 0.24. We used 14 g of bare foam. The density of the bare foam, before the expansion, is ≈ 1 g/ml. The total volume of the plastic tubes, where we pour the PG foam, is 58 ml.

The theoretical value of the magnetic susceptibility of the PG microparticles is -204 ppm, which we calculated at the beginning of this chapter. The theoretical value lies within

the uncertainty range of our experimental result. Moreover, we find that the magnetic susceptibility of the bare foam is similar to the one of water. This result is in good agreement with values found in literature for the magnetic susceptibility of polyurethane foams [32]. This reassures the reliability of the experiment.

3.3.3 In vivo Experiments

We present the results of the *in vivo* experiments to evaluate the effectiveness the PG foam neck shim. The PG foam neck shim has a 4% volume fraction of PG microparticles, which implies a final magnetic susceptibility close to the one of water. In figure 3.7a and 3.7b we show the *in vivo* B_0 field maps through the sagittal plane without foam and with the PG foam neck shim, respectively. In these images, there are some phase wrapping artifacts, which is a commonly encountered problem in B_0 field mapping [9]. The data obtained from the MR scanner is in Hertz, which differs from the B_0 field inhomogeneities by a scaling factor. We transform this data to B_0 inhomogeneities (in ppm), using this formula: $\Delta B_0 = \frac{\Delta \nu 2\pi}{\gamma}$, where $\Delta \nu$ is difference in phase (Hertz) and γ is the gyromagnetic ratio of the proton.

In order to quantitatively measure the B_0 main field in the region of the neck with and without PG foam, we plot values from the shoulders to the brain throughout a line, i.e., fixing x and y dimensions while taking values along the z direction from the shoulders to the neck (black lines in figure 3.7a and 3.7b). The PG foam acts as a susceptibility matching material effectively moving the air-tissue field gradient outside the subject's body. The inhomogeneity of the B_0 field is improved, as shown in figure 3.3c, where it is plotted the *in vivo* B_0 field along a line without PG foam (red) and with PG foam (blue).

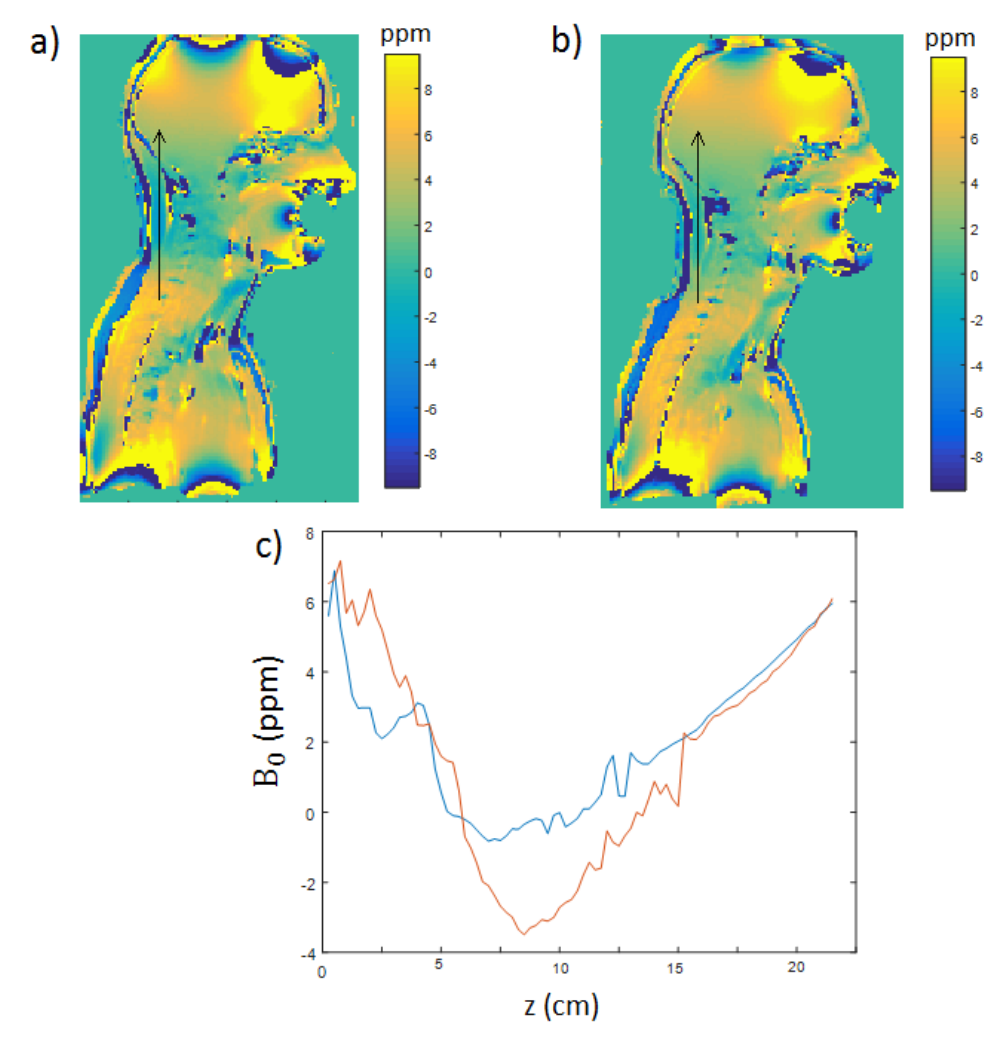


Fig. 3.7 B_0 field maps (sagittal view) without foam (a) and with PG foam neck shim (b). The two images are acquired with a gradient echo sequence in a 3T MR scanner. FOV= 32×48 cm² and TR= 10 ms. The slice thickness is 2 cm and the echo time is 1.23 ms. The difference between echo times is 0.8 ms. The black line represents the region we considered for the analysis of the B_0 field values in (c). Here it is shown the B_0 field along the z direction, from the shoulders to the brain along the black line in the field maps. The blue line represents the case where the subject has a PG foam around the neck, the red line, however, represents the case without the foam. The dip in the B_0 field is smaller when the PG foam is used. This implies that the perturbations arising from the air-tissue interface in the neck are slightly corrected using the PG foam.

In order to confirm the trustworthiness of our experimental results, we compare the *in vivo* results with simulations using MATLAB. We simulate a neck shim with a similar shape to the one we built and with a magnetic susceptibility of -9 ppm. For our simulations we use a male body model [19]. In the following figures 3.8a and 3.8b, we show the simulated B_0 field maps without PG foam and with a PG foam. In figure 3.8c, we plot the B_0 field

along a line for both cases.

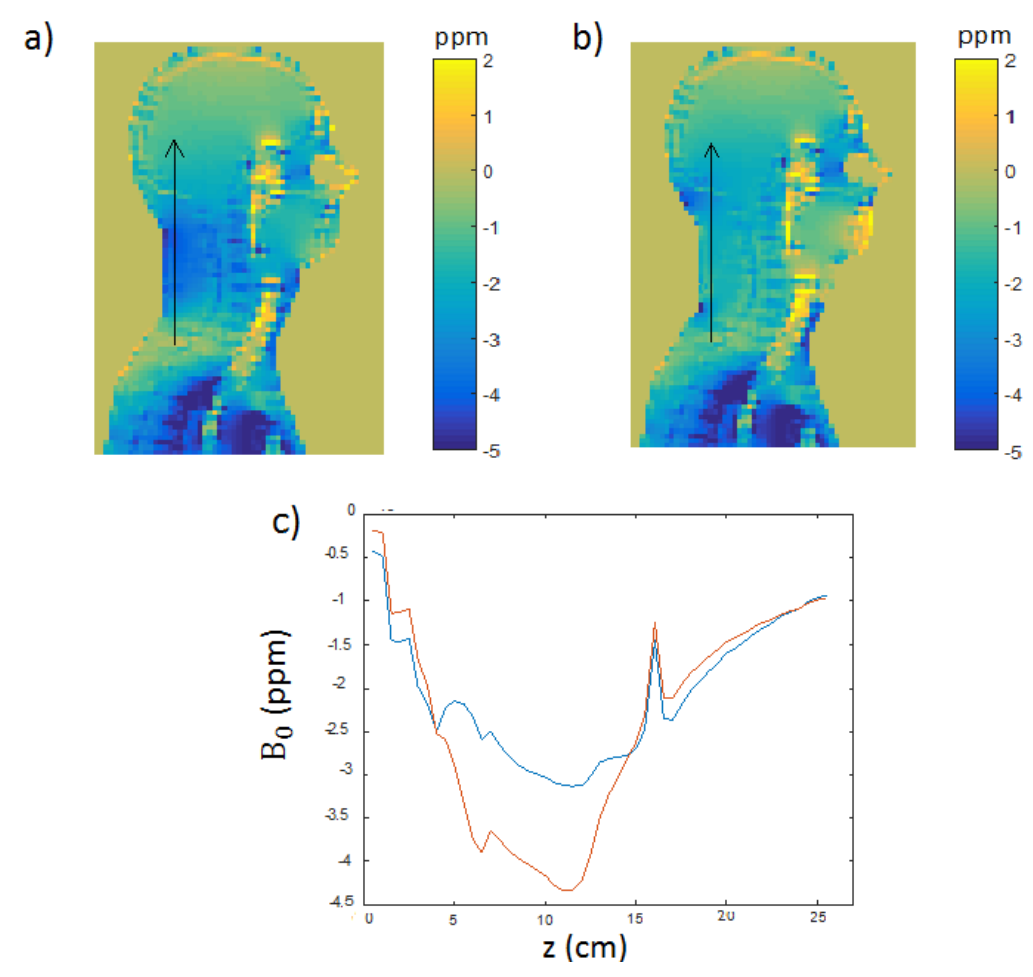


Fig. 3.8 Simulations of the B_0 field inhomogeneities in a human body model (sagittal view) without PG foam (a) and with PG foam surrounding the neck (b). The B_0 field is measured in ppm-s. The black line represents the region we considered for the analysis of the B_0 field values in (c). Here it is shown the B_0 field along the z direction, from the shoulders to the brain. The blue line represents the case where the subject has a PG foam around the neck, the red line, however, represents the case without the foam. The PG foam improves the uniformity of the B_0 field as expected

There is a clear correlation between the *in vivo* B_0 plot in figure 3.7c and the one obtained with simulations in figure 3.8c. This demonstrates that the experimental results are in good agreement with simulations. It should be noted that the simulations show a slight better improvement of the B_0 inhomogeneities rather than the *in vivo* results. This could be due to small air-gaps between the subject's neck and the PG foam neck shim.

In conclusion, the B_0 inhomogeneities near the skin are reduced using a PG foam neck shim with a 4% volume fraction of PG powder. The PG foam is simple to shape and

lightweight. Another benefit of the PG foam neck shim is that it can be embedded within an RF coil, allowing for localized B_0 shimming at the same time. Furthermore, the SNR does not decrease using PG foams. The experimental results of the B_0 field maps are in agreement with the simulations, thus implying a reliable performance of the PG foam neck shim.

Chapter 4

Optimum PG Foam Design: a Numerical Study

In the previous chapter we investigate the effect of the PG composite foam for B_0 passive shimming from a mostly experimental viewpoint. We would like to go one step further and find the optimum design of a PG foam that homogenizes the B_0 field most efficiently. To do so, we investigate the B_0 passive shimming problem from a more mathematical and computational viewpoint. In this chapter we preset a numerical algorithm which generates the optimum design for a shim that homogenizes the B_0 field in a desired ROI. First, we present the mathematical modeling used for the design of the shim. Then, we present the results of a neck shim and we discuss the benefits and drawbacks of the algorithm.

4.1 Mathematical Modeling

This section presents the basic ideas of the mathematical modeling which could be used to optimally design a PG foam. The goal is to obtain the optimum design for a shim which is able to homogenize the B_0 main static magnetic field in specific regions of the human body. The design must be efficient and applicable, i.e. not only it must homogenize the magnetic field in the ROI, but it also must be experimentally implementable. We begin by explaining the forward problem (also called direct problem) for which we present a different method from the general approach that uses Fast Fourier Transforms (FFT). Next, we explain the inverse problem framework. Then, we explain the gradient descent algorithm, which provides us with the least square solution (LSQ) to the inverse problem. This solution takes all type of values as it is defined without any constraint. In order to find a solution under some imposed constraints, we integrate a level set-based topology optimization approach into the gradient descent algorithm. We outline the concept of reinizialization as it is an essential part for the performance of the algorithm. We finish this chapter proposing a way to reduce the computation time of the algorithm.

4.1.1 B_0 modeling: the forward problem

The goal is to design a shim that creates a magnetic field which compensates for the B_0 field inhomogeneities generated by the susceptibility distribution of the human body. We will approach this problem as a domain decomposition scheme [39]. The final total field can be decomposed into a primary field $\Delta B(\vec{r})_{\text{body}}$, produced by the human body magnetic susceptibility distribution (without foam shim) and a secondary field $\Delta B(\vec{r})_{\text{f}}$, produced by the magnetic susceptibility distribution of the PG foam shim. A schematic illustration of the domain decomposition method is given in the following figure.

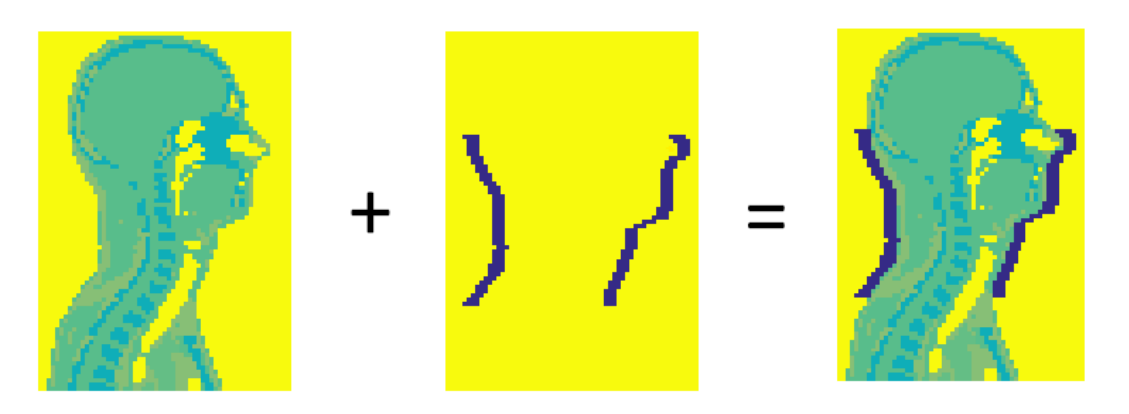


Fig. 4.1 Illustration of the domain decomposition from the sagittal view. The total susceptibility (right) is the sum of the susceptibility generated by the human body (left) and the PG foam shim (center).

As mention in section 2.2, a susceptibility distribution generates non-uniformities in the B_0 field. In the spatial domain, the B_0 field perturbation, given in tesla units, induced by the magnetic susceptibility of a foam (χ_f) is [22]:

$$\Delta B_{\rm f}(\vec{r}) = B_0 \int_{r' \in D_{\rm f}} G(\vec{r} - \vec{r'}) \cdot \chi_{\rm f}(\vec{r'}) d\vec{r'}$$
(4.1)

In this expression $\vec{r} = (x, y, z)$ denotes the position vector: $\vec{r} \in D_{\text{ROI}}$. D_{ROI} is the spatial domain that encompasses the ROI. D_{f} , however, is the spatial domain that encompasses the foam and $r' \in D_{\text{f}}$. Note that D_{ROI} and D_{f} need not to be coincident and can be at a distance from each other [40]. Furthermore, the Green's function of the system is denoted by $G(\vec{r} - \vec{r'})$ and it relates the magnetic susceptibility distribution of the foam to the generated magnetic field perturbation in the ROI [20,21]. The Green's function is independent of the foam susceptibility value or geometry; it represents the sensitivity of the B_0 field to any foam. The background B_0 field is outside the integral because it is not position dependent.

The equation 4.1 represents a mathematical operation known as convolution [41], which can also be denoted with the symbol \otimes . Moreover, by dividing the field inhomogeneities

with the B_0 main field, we represent $\Delta B_{\rm f}(\vec{r})$ in parts per million (ppm). Hence, the following expression is equivalent to equation 4.1 but in ppm units:

$$\Delta B_{\rm f}(\vec{r}) = G(\vec{r}) \otimes \chi_{\rm f}(\vec{r}) \tag{4.2}$$

Throughout the thesis the field inhomogeneities are expressed in ppm unless the contrary is clearly stated.

A very popular approach to solve this problem is by using Fast Fourier Transforms. By applying the convolution theorem [41] to equation 4.2, efficient FFT-s may be used to improve computation speed [20,21]. This leads to the equations 2.14 and 2.15 in chapter 2. This method has been extensively evaluated [20,21,40,42,43]. In spite of being a valuable tool in the prediction of the B_0 field perturbations generated by magnetic susceptibility distributions, the FFT method requires that the quantities being numerically convolved have the same matrix size and consistent coordinate axes. Nevertheless, we want to reduce the problem region and perform a volume of interest based approach [22]. This method would imply lower memory requirements [22]. The method we propose does not need the use of Fourier Transforms. The magnetic field inhomogeneities are expressed in the following matrix manner:

$$\begin{pmatrix}
\Delta B_{\mathbf{f}}(r_1) \\
\vdots \\
\Delta B_{\mathbf{f}}(r_n)
\end{pmatrix}_{n \times 1} = \begin{pmatrix}
G(r_1 - r'_1) & \cdots & G(r_1 - r'_m) \\
\vdots & \ddots & \vdots \\
G(r_n - r'_1) & \cdots & G(r_n - r'_m)
\end{pmatrix}_{n \times m} \begin{pmatrix}
\chi_{\mathbf{f}}(r'_1) \\
\vdots \\
\chi_{\mathbf{f}}(r'_m)
\end{pmatrix}_{m \times 1}$$
(4.3)

The size of the G matrix (n × m) is the number of points in the ROI (n) times the number of points in the foam design domain (m). In our method, the value of G at each point in the design domain is different. This spatial Green's function is subject to the design domain, $D_{\rm f}$ and the spatial domain of the ROI, $D_{\rm ROI}$.

4.1.2 Inverse Problem Framework

Associated with any forward problem there is an inverse problem. In the case of B_0 shimming, the forward problem seeks to determine the magnetic field inhomogeneities generated by an object with a certain susceptibility distribution, i.e., it calculates some physical response. The inverse problem, however, consists in determining the properties of the object given the (desired) generated magnetic field. There is a variety of inverse problems and optimal design problems, where the unknown variable is a geometric object, whose topology is unknown. The direct problem is usually well-posed, whereas the inverse problem is usually ill-posed. In order to briefly explain the ill-posedness concept, we use a linear operator equation Ax = b, as an example. A is a bounded linear operator $A: H \to K$, which maps from a Hilbert space H to a Hilbert space K. The forward problem is defined as finding b assuming x is known, while the inverse problem is defined as finding x from the knowledge of b. The problem is well-posed if there exists only an exact solution and it depends continuously on the data [46]. One consequence of these statements is that A^{-1} must exist. Our inverse problem, as most of the inverse problems

encountered in physics, do not satisfy these requirements. Hence, we are dealing with an ill-posed problem. As we cannot directly invert the matrix A, we use methods from optimization to solve the inverse problem.

In our inverse problem, the known parameters are: the magnetic field perturbations that we want to correct $(\Delta B_{\rm f}(\vec{r}))$, the applied main static magnetic field (B_0) and the Green's function of the system $(G(\vec{r}, \vec{r'}))$. The unknown parameter that we want to solve for is the magnetic susceptibility distribution of the foam $(\chi_{\rm f}(\vec{r'}))$. In summary, for a given field, a solution is sought in terms of the foam.

We define the cost function as a functional that measures the difference between the desired $\Delta B(\vec{r})$ and the actual one. The method is formulated by minimizing the cost function, denoted by F. Defining \mathbf{P} , \mathbf{G} , $\chi_{\mathbf{sf}}$, $\Delta \mathbf{B_{target}}$ and \mathbf{F} as matrices, the cost function is given by:

$$\mathbf{F} = \|\mathbf{G}\chi_{\mathbf{f}} - \mathbf{\Delta}\mathbf{B}_{\text{target}}\|_{D_{ROI}}^{2} \tag{4.4}$$

 $\Delta B_{\mathrm{target}}(\vec{r})$ is the ideal magnetic field that we want the foam to generate in order to fully compensate for the inhomogeneities generated by the body, hence: $\Delta B_{\mathrm{target}}(\vec{r}) = -\Delta B_{\mathrm{body}}(\vec{r}) + \mathrm{Const.}$ The constant is just an offset, which can be determined during the scanner. We want the final total magnetic field to be homogeneous, i.e., to be either zero or a constant.

We need to find a solution for $\chi_f(\vec{r'})$ that minimizes F and that can be implemented using a PG foam. In the following sections, we explain the gradient descent algorithm and level set-based topology optimization. First, the gradient descent algorithm provide us with a solution for $\chi_f(\vec{r'})$ that minimizes the cost function. Next, the level set method is used to optimize the material layout within a given design domain, boundary conditions and constraints. In this way, we can impose the system to give a solution for the magnetic susceptibility distribution of the foam, which we can also practically implement.

4.1.3 Gradient Descent Algorithm

The gradient descent is an algorithm that finds the minimum of a function by using iterative optimization. We consider our function to be defined by a set of parameters. The gradient descent starts with an initial set of parameter values and iteratively moves toward a set of parameter values that minimize the function. To attain a minimizer, steps should be taken in the negative direction of the gradient of the function [47]. We assume our initial point to be $\chi^{(k)}$. To find a point $\chi^{(k+1)}$ (which is closer to the minimizer than the initial point), we start at $\chi^{(k)}$ and move by an amount $-\beta_k \nabla \mathbf{F}$. $\beta_k > 0$ is the time-step in the k^{th} iteration and $\nabla \mathbf{F}$ is the gradient of the cost function. This is expressed by the following iterative algorithm [47]:

$$\chi^{(k+1)} = \chi^{(k)} - \beta_k \nabla \mathbf{F}(\chi), \tag{4.5}$$

where the β_k represents the magnitude of the update in step k.

The gradient descent algorithm provides us with the least square solution to the inverse problem. It should be noted that there are other methods to obtain a least square solution. One of the common methods to find a solution to an inverse problem is by using the Moore-Penrose pseudoinverse matrix. Nevertheless, we use the gradient descent algorithm because it allows us to incorporate constraints. The values of the least square solution may be arbitrary, i.e., we do not have any control over the values that the solution takes. However, we are looking for a solution which is not only effective, but also experimentally applicable. Therefore, we implement the gradient descent algorithm together with a numerical technique called level set method, so that we can iteratively update the geometry of the foam shim under specific constraints as to what values can be attained.

4.1.4 Level Set Methodology Integrated into a Gradient Descent Algorithm

The level set method was first described by Osher and Sethian in 1998 [44] as a versatile method for representing an interface in two or three dimensions. In the level set method the shape of an object is represented implicitly by one higher-dimensional level set function. The outer limit of the shape coincides with the zero level of this function, and the interior of the shape is defined by the positive values of the level set function. Figure 4.2 illustrates this relationship. Moreover, with the level set method topological discontinuities are well defined and easily performed which is of great advantage [45].

The inverse problem that we are dealing with can be stated in the following way [48]:

Find Ω in the equation

$$\min \mathbf{F}(\chi_{\mathrm{f}}),$$

where

$$\chi_{\rm f}(x) = \begin{cases} \chi_{\rm int} & \text{for } x \in \Omega \\ \chi_{\rm ext} & \text{for } x \notin \Omega \end{cases}$$

The domain Ω is the desired unknown, $\Omega \subset \mathbb{R}^n$, i.e., in our case the desired geometry of the foam. χ_{int} is the magnetic susceptibility value of the PG foam and χ_{ext} indicates the no material region: $\chi_{\text{ext}} = 0$. Note that $x = (x_1, ..., x_n) \in \mathbb{R}^n$.

Let $\partial\Omega$ be the boundary of Ω (fig. 4.2(b)). The level set method uses an auxiliary function ϕ , called the level set function, to represent the interface $\partial\Omega$ as the set where $\phi(x) = 0$. Here $x = (x_1, ..., x_n) \in \mathbb{R}^n$. Hence, $\partial\Omega$ is represented as the the zero level set of ϕ by:

$$\partial\Omega(t) = \{x|\phi(x) = 0\} \tag{4.6}$$

Accordingly, the level set method implicitly manipulates the function $\partial\Omega$ through the level set function ϕ . The latter one is positive inside Ω , negative outside Ω and zero inside

 $\partial\Omega$. Under this description, we can state the inverse problem in a more convenient way [48]:

Find ϕ in

$$\chi_{\rm f}(x) = \begin{cases} \chi_{\rm target} & \{x : \phi(x) > 0\} \\ 0 & \{x : \phi(x) \le 0\} \end{cases}$$

such that

$$\min \mathbf{F}(\chi_{\mathrm{f}})$$

The expression for the $\chi_{\rm f}$ is the equivalent to the Heaviside function of ϕ :

$$\chi = \chi_{\text{target}} H(\phi), \tag{4.7}$$

where the Heaviside function $H(\phi)$ is defined by:

$$H(\phi) = \begin{cases} 1 & \text{if } \phi > 0 \\ 0 & \text{if } \phi \le 0 \end{cases}$$

Representing the unknown foam geometry Ω through the level set function ϕ provide us with a great advantage: there is no need to make any assumption about the nature and topology of Ω , such as whether Ω is composed by connected subregions or it is homogeneous [48].

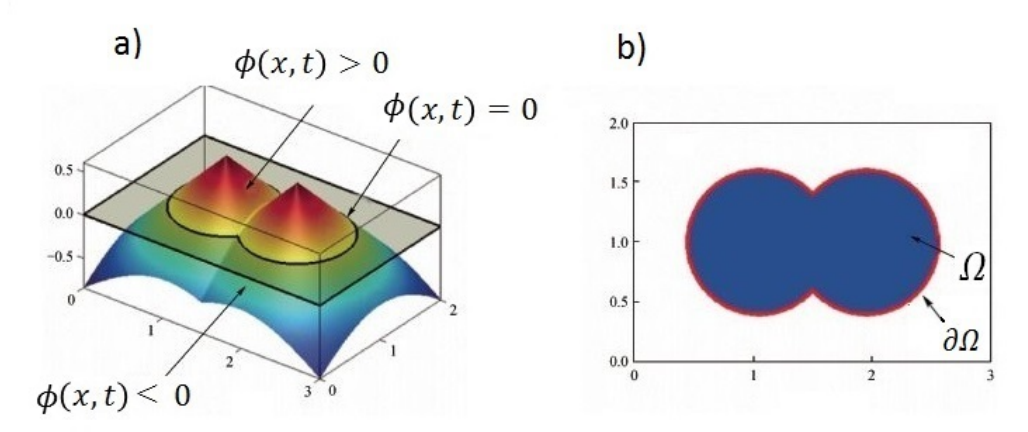


Fig. 4.2 Figure taken from reference [49]. Level set representation of a 2D structure. (a) The level set method. (b) Design domain.

Our aim is to combine the level-set based topology optimization approach and the gradient descent algorithm to find a solution that complies with our constraints. Following equation 4.5, the level set function iteratively updates as:

$$\phi^{(k+1)} = \phi^{(k)} - \beta^{(k)} \frac{dF}{d\phi}$$
 (4.8)

In this way, the level set function reduces, and eventually minimizes, the cost functional.

The gradient of F, $\frac{dF}{d\phi}$, must be chosen such that the cost functional F decreases in each iteration. By using the chain rule, we formally differentiate the cost functional $F(\chi(\phi))$ with respect to ϕ [50].

$$\frac{dF}{d\phi} = \frac{\partial F}{\partial \chi} \frac{\partial \chi}{\partial \phi} = \frac{\partial (\|G\chi - B\|^2)}{\partial \chi} \frac{\partial (\chi_{\text{target}} H(\phi))}{\partial \phi}$$
(4.9)

In order to solve the first partial derivative $\frac{\partial F}{\partial \chi}$ we make use of the *Fréchet Derivative*, which is implicitly defined through the following relation [51, 52]:

$$\lim_{\|h\|\to 0} F(\chi+h) - F(\chi) - \operatorname{Re}\langle \frac{\partial f}{\partial \chi}, h \rangle = 0 \tag{4.10}$$

Next, by substituting $h = t\phi$ and taking the limit $t \to 0$ instead, we find:

$$\operatorname{Re}\langle \frac{\partial F}{\partial \chi}, \phi \rangle = \lim_{\|t\| \to 0} \frac{F(\chi + t\phi) - F(\chi)}{t}$$

$$= \lim_{\|t\| \to 0} \frac{\|G(\chi + t\phi) - B\|^2 - \|G\chi - B\|^2}{t}$$

$$= \lim_{\|t\| \to 0} \frac{\|G\chi + Gt\phi - B\|^2 - \|G\chi - B\|^2}{t}$$

$$= \|G\chi - B\|^2 + \langle G\chi - B, G\phi \rangle + \langle G\phi, G\chi - B \rangle - \|G\chi - B\|^2$$

$$= 2\operatorname{Re}\langle G\chi - B, G\phi \rangle$$

$$= 2\operatorname{Re}\langle G^*(G\chi - B), \phi \rangle,$$
(4.11)

where G^* is the complex conjugate transpose of the Green's function matrix G.

From this relation we find the gradient of the cost function to be:

$$\frac{\partial F}{\partial \chi} = G^*(G\chi - B) \tag{4.12}$$

Using the expression for $\frac{\partial F}{\partial \chi}$ we have just obtained and taking into account that the derivative of a Heaviside function is a Dirac delta function, we get:

$$\frac{dF}{d\phi} = G^*(G\chi - B)\chi_{\text{target}}\delta(\phi), \tag{4.13}$$

where $\delta(\phi) \equiv \frac{dH(\phi)}{d\phi}$.

Therefore, the update rule is given by:

$$\phi^{(k+1)} = \phi^{(k)} + \beta_k (G^*(G\chi - B)\chi_{\text{target}}\delta(\phi))$$
(4.14)

We still need to find out the stepsize β_k , which represents the magnitude of the update in step k. The optimal stepsize is found by minimizing the cost function in the k^{th} iteration for a variation in β_k : $\min_{\beta_k} F$. In other words, β_k satisfies the following equation [52]:

$$\frac{\partial F}{\partial \beta_{\mathbf{k}}} = 0 \tag{4.15}$$

The mathematical derivation of the equation above is outside the scope of this thesis. In our numerical algorithm we use the embedded Matlab function *fminsearch* (see Appendix A). The reader seeking an in-depth understanding of the level set methods may refer to more advanced books such as [53,54].

Smooth approximations to H, δ and S functions

For level sets that iteratively update, it is necessary to replace the Heaviside function H and the delta function δ by some smooth equivalent functions. In numerical implementations, it is beneficial to use epsilon-approximations to these equations in order to avoid outcomes as zero or infinity. In our simulations, the following smooth functions are used to replace H and δ [57]:

$$H_{\epsilon}(\phi) = \frac{1}{\pi} \arctan \frac{\phi}{\epsilon} + \frac{1}{2} \tag{4.16}$$

$$\delta_{\epsilon}(\phi) = \frac{\epsilon}{\pi(\phi^2 + \epsilon^2)},\tag{4.17}$$

where ϵ is sufficiently small.

Reinizialization

While equation 4.14 implicitly updates the object boundary $\delta\Omega$ by a level set function ϕ , this can become irregular after some number of iterations [55]. The level set function can become really flat and this can lead to high numerical errors [56]. In other words, if the gradient of ϕ is very small around the interface, the Heaviside function is not well defined. This implies that $\chi_f(\phi)$ will take not only the values of zero and χ_{target} , but also the values in between. A simple example is illustrated in figure 4.3.

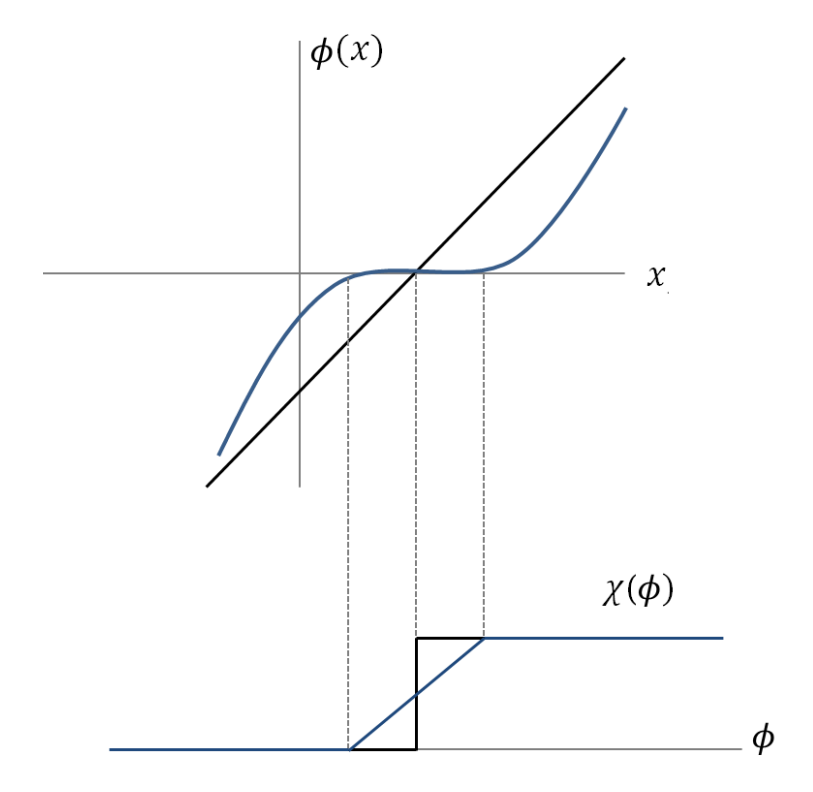


Fig. 4.3 In the top figure, two level set functions are plotted. The black line represents a simple example of a non-irregular level set function $\phi(x)$. Its slope is constant. The blue line represents an irregular level set function: in the point where $\phi = 0$ is it very flat. In the bottom figure, the $\chi(\phi) = H(\phi)$ is plotted. The χ_{black} , which represents the Heaviside function of ϕ_{black} is well defined, i.e., $\chi(\phi)$ can only take two values. However, the χ_{blue} , which represents the Heaviside function of ϕ_{blue} , is not well defined, i.e., $\chi(\phi)$ can take more than two values.

To maintain a regular shape for the level set function and to assure reliable results, reinizializing the level set function becomes a crucial step in the level set methodology. We need to assure that the absolute value of the gradient of the level set function remains unity [55]:

$$|\nabla \phi(x)| = 1 \tag{4.18}$$

If the gradient of the level set function has a value of unity around the interface, this would imply that the level set function does not become very flat or steep and χ_f will take only the assigned values zero or χ_{target} , which is what we are aiming for. We can use an iterative process to change ϕ until its gradient gives unity. This can be formulated mathematically as follows [55]:

$$\phi_{j+1} = \phi_j + S(\phi_0)(|\nabla \phi| - 1), \tag{4.19}$$

where ϕ_0 is the starting level set function [55] and S is the sign function.

For the numerical implementation, it is necessary to smooth the sign function as [55]:

$$S(\phi_0) = \frac{\phi_0}{\sqrt{\phi_0^2 + \epsilon^2}},\tag{4.20}$$

where ϵ is sufficiently small.

4.1.5 Subdomains to increase the speed of the algorithm

The level set method may be a very powerful tool to solve the optimization problem. However, the minimization problem can be composed by a very large system of equations, i.e. the parameters of eq. 4.4 may involve very big matrices. The computation time to solve these system of equations using the previously explained level set method can become prohibitive. In this section we present a method to make the algorithm faster and simpler by using subdomains. In the numerical results presented in this thesis (section 4.2) we did not use this subdomain approach as the computation time for our ROI was not excessively large. We believe that this method could potentially be implemented in topological optimization problems, leading to a fast and efficient performance of the algorithm. We consider it worthwhile to briefly explain the idea behind the method in this section, as it may be beneficial for future research.

The subdomain approach is based on replacing the total magnetic susceptibility of the foam $\chi_{\rm f}(\vec{r'})$ with a reduced magnetic susceptibility $\chi_{\rm sf}(r')$ and a matrix P. The following expression is the matrix representation of the subdomain approach.

$$\begin{pmatrix} P(r'_1, r'_1) & \cdots & P(r'_s, r'_1) \\ \vdots & \ddots & \vdots \\ \vdots & & & \vdots \\ P(r'_1, r'_m) & \cdots & P(r'_s, r'_m) \end{pmatrix}_{m \times s} \begin{pmatrix} \chi_{\text{sf}}(r'_1) \\ \vdots \\ \chi_{\text{sf}}(r'_s) \end{pmatrix}_{s \times 1} = \begin{pmatrix} \chi_{\text{f}}(r'_1) \\ \vdots \\ \vdots \\ \chi_{\text{f}}(r'_m) \end{pmatrix}_{m \times 1}$$
(4.21)

P is a matrix with only values zero and one. The size of the P matrix (m \times s) is the number of points in the foam design domain (m) times the number of subdomains (s). In the first column of P the elements belonging to the first subdomain take the value one and all others zero, in the second column the elements belonging to the second subdomain take the value one and all the others zero and so forth. $\chi_{\rm sf}$ is the reduced magnetic susceptibility vector of the foam and its length is the number of subdomains (s). Hence, by multiplying this matrix with the reduced $\chi_{\rm sf}$ we recover the total $\chi_{\rm f}$ of the system.

Next, we use this equality for the minimization problem of the cost function F (eq. 4.4). Defining \mathbf{P} , \mathbf{G} , $\chi_{\mathbf{sf}}$, $\Delta \mathbf{B}_{\mathbf{target}}$ and \mathbf{F} as matrices, we write:

$$\min_{n \times 1} \mathbf{F} = \min \| \mathbf{G}_{n \times m} \cdot \mathbf{P}_{m \times s} \cdot \chi_{sf} - \Delta \mathbf{B}_{target} \|_{D_{ROI}}^{2}$$

$$(4.22)$$

In this equation the symbol \cdot represents the matrix multiplication. $\mathbf{G} \cdot \mathbf{P}$ can be regarded as the reduced Green's function of the system.

It should be emphasized that after this replacement, the unknown parameter of the inverse problem is not the total magnetic susceptibility of the foam anymore, but the reduced one $(\chi_{\rm sf})$. As a consequence, the system of equations that the level set has to solve reduces considerably. The speed of the algorithm increases depending on the chosen amount of subdomains, i.e. the more subdomains, the smaller the size of $\chi_{\rm sf}$ and the faster the inverse problem is solved. Using the subdomain approach we loose resolution and accuracy in our solution. Nevertheless, this lost in precision does not have a negative effect in the final outcome, as we do not need high resolution for our practical $\chi_{\rm f}(\vec{r'})$. Therefore, the subdomain approach reduces the complexity of the problem and it is an advantage both for the computation time and applicability of the solution.

4.2 Results and Discussion

In this chapter, we present the results of the numerical simulations to obtain an optimum design of one PG foam. We present results using both a gradient descent algorithm (without constraints) and an optimized algorithm that consists of level sets integrated into a gradient descent iterative minimization. The Matlab code of the latter algorithms is included in the Appendix A. Our aim is to find a optimum design of a shim that compensates the B_0 field inhomogeneities in the neck generated by the different magnetic susceptibilities of the body. For our simulations the following parameters should be considered:

- **Design domain**. A design for the PG foam shim is sought for the design domain $D_{\rm f}$. In our case, we choose a design domain that covers the human body from the eyes to the shoulders, as shown in figure 4.1 (center).
- ROI. D_{ROI} is the spatial domain in which we are trying to homogenize B_0 . We chose the ROI to be the neck, as there are strong B_0 field perturbations. The ROI chosen for our simulations is shown in the following figure.

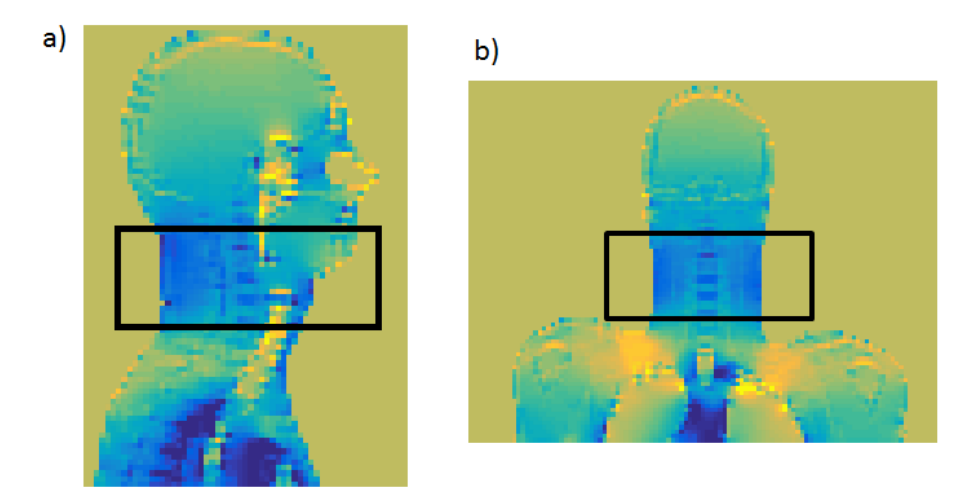


Fig. 4.4 Simulation of the B_0 field inhomogeneities generated in the upper part of the human body in the sagittal view (a) and coronal view (b). The part inside the black square is the region that we want to homogenize, i.e., the ROI.

- Green's function. The spatial Green's function relates the geometry and values of the foam to the magnetic field correction in the ROI.
- B_0 target. It must be a constant value. In this case, we chose the final value for the B_0 in the ROI to be zero. This means that we want to find a shim that fully compensates for the inhomogeneities in the neck and provides a final $B_0 = 0$.
- **Number of iterations**. The maximum number of iterations to find a solution to the inverse problem.
- Initial χ_f . Only used in the gradient descent algorithm. We chose the initial value of the function χ_f to have all elements zero.
- Initial ϕ . Only used in the level set algorithm. We chose the initial value of the level set function ϕ to have all elements zero. The reason to choose a zero matrix is that the derivative of the Heaviside function is maximal when the level set function is zero. Therefore, this will introduce updates throughout the design domain.
- χ_{target} . Only used in the level set algorithm. It is the susceptibility value that we want the shim to have. In our simulations we use $\chi_{\text{target}} = -10$ ppm. The reason to choose -10 ppm of magnetic susceptibility for our shim is that we have already experimentally construct a PG foam with such magnetic susceptibility value, experimentally demonstrating that it improves the uniformity of the B_0 field. Hence, -10 ppm is a realistic and experimentally practical value.
- ϵ . Only used in the level set algorithm. It is used for the smooth approximations of the Heaviside function and the Dirac delta function (equation 4.16 and 4.17). In

our simulations we iteratively decrease the value of epsilon. In this way, we allow the system to make more updates at the beginning and the constraints get gradually imposed. Typically, we give an initial $\epsilon=0.9$ and it decreases five to six orders of magnitude.

• Reinizialization. For the reinizialization of the level set function we use the Matlab toolbox by Baris Sumengen [59]. Parameters used are: alpha=0.7, iterations= 10 and accuracy= 'ENO3'.

Gradient descent algorithm

First, we present the results from the simulations using the gradient descent algorithm. The initial value for the function χ_f is a zero vector. In every iteration the cost function decreases as the algorithm approaches a better solution to the inverse problem (fig. 4.5a). Using a gradient descent algorithm the final susceptibility can take all values as we are not imposing any constraint (fig. 4.5b).

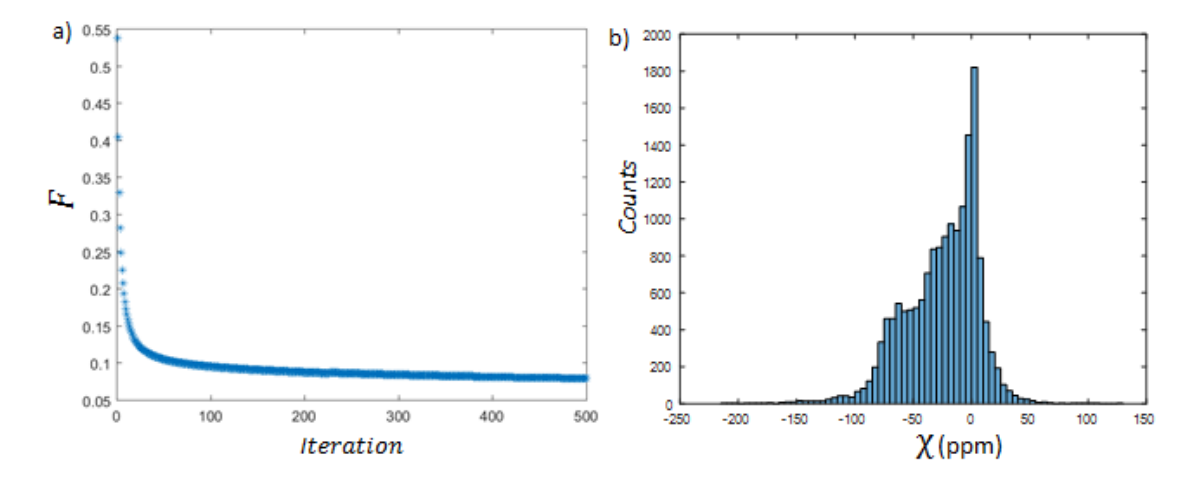


Fig. 4.5 (a) Cost function versus the number of iterations. The cost function decreases iteratively. Maximum number of iterations: 500. (b) Histogram of the values for the magnetic susceptibility of the foam χ_f .

In figure 4.6, B_0 field perturbations produced by the human body (a) and the magnetic field produced by the LSQ solution (b) are shown. The total final magnetic field (c) is the sum of the previous two, and it shows a corrected B_0 field in the neck. Thus, it demonstrates that the gradient descent algorithm efficiently homogenizes the ROI.

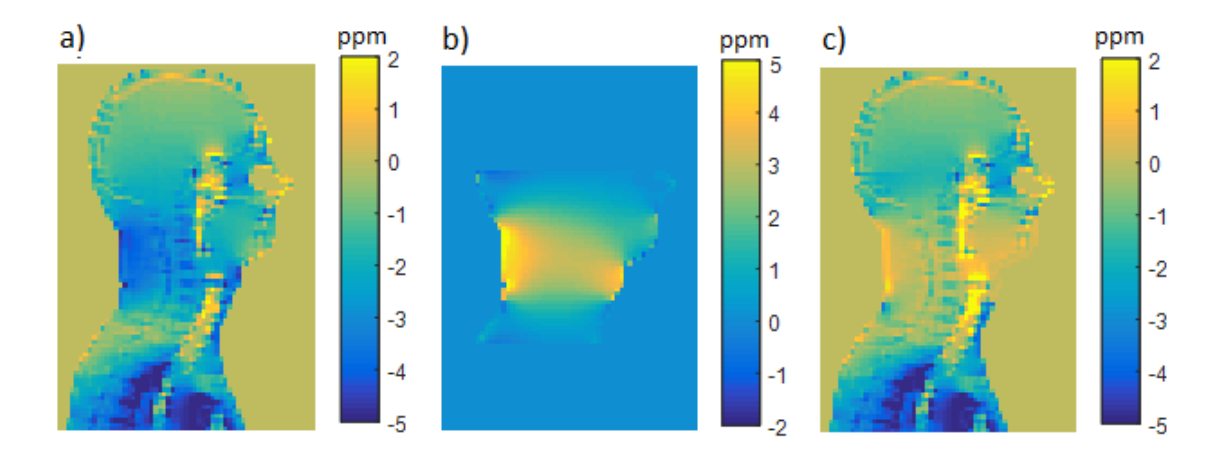


Fig. 4.6 (a) Magnetic field inhomogeneities produced by the human body. (b) Magnetic field produced by the LSQ solution for the neck shim, which should be able to compensate the inhomogeneities in the ROI. (c) Final magnetic field, which is the sum of the B_0 inhomogeneities generated by the human body and magnetic field generated by the LSQ solution for the neck shim.

The results show that LSQ solution for the design of the PG foam is very effective, i.e., the B_0 field in the ROI becomes very homogeneous. However, the practical implementation of this design is impossible: the magnetic susceptibility takes values from -100 ppm to 50 ppm (fig. 4.5b). This design is not experimentally applicable. As a consequence, we need to give some constraints to the system. This is achievable by using the level sets, which results will be discussed next.

Level set optimization integrated into a gradient descent algorithm

By implementing the level set method into the above algorithm, the results we obtain are subject to our desired constraints, i.e., the final susceptibility distribution can only take two values, either zero or χ_{target} . As a consequence, the final solution for the magnetic susceptibility of the PG foam becomes experimentally implementable. The design domain covers the entire region from the eyes to the shoulders (fig. 4.7a). The level set algorithm reconstructs the geometry of the neck shim (fig. 4.7b) such that it fulfills the imposed requirements. This is demonstrated in figure 4.8b, where the histogram of the values for the magnetic susceptibility of the foam is plotted. In contrast with the LSQ case, the final values for $\chi_{\rm f}$ can only be zero or $\chi_{\rm target} = -10$ ppm.

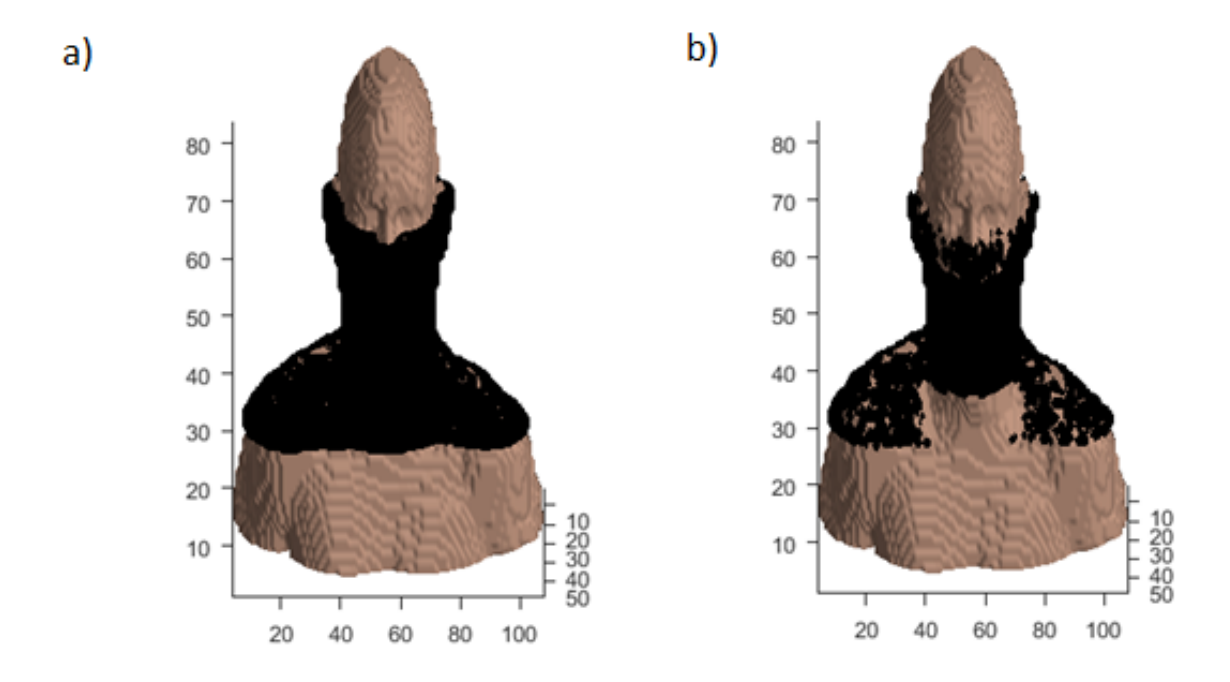


Fig. 4.7 (a) Design domain. (b) Reconstructed geometry by the level set algorithm.

The reconstructed geometry for the neck shim fully covers the entire region of the neck, while partially covering the shoulders (figure 4.7b). We believe that the reconstructed shim has a reasonable shape. In the remaining of this paragraph, we give an intuitive and qualitative explanation for this statement. We may view the shim as a three dimensional grid composed by individual elements, each one being a magnetic susceptibility point in space. Hence, each element of the grid generates a magnetic field and the total field generated by the shim will be the sum of all of them. Each source susceptibility region generates a magnetic field with a shape of the well-known dipole pattern, with positive and negative lobes [22], as it is shown in figure 2.4. A point source with a negative magnetic susceptibility generates main lobes that are negative and side lobes that are positive. When all these elements are placed around the neck, the positive lobes are the ones contributing the most to the generated magnetic field in the neck. Hence, the generated field correction is positive and it compensates for the B_0 field perturbations in the neck (figure 4.9). Therefore, we expect the design to be filled with material around the neck, as we obtain in the numerical simulation. The other regions of the design domain have a smaller effect in the homogenization of the B_0 field of the ROI and that is why they are partially filled with material or they do not have material at all.

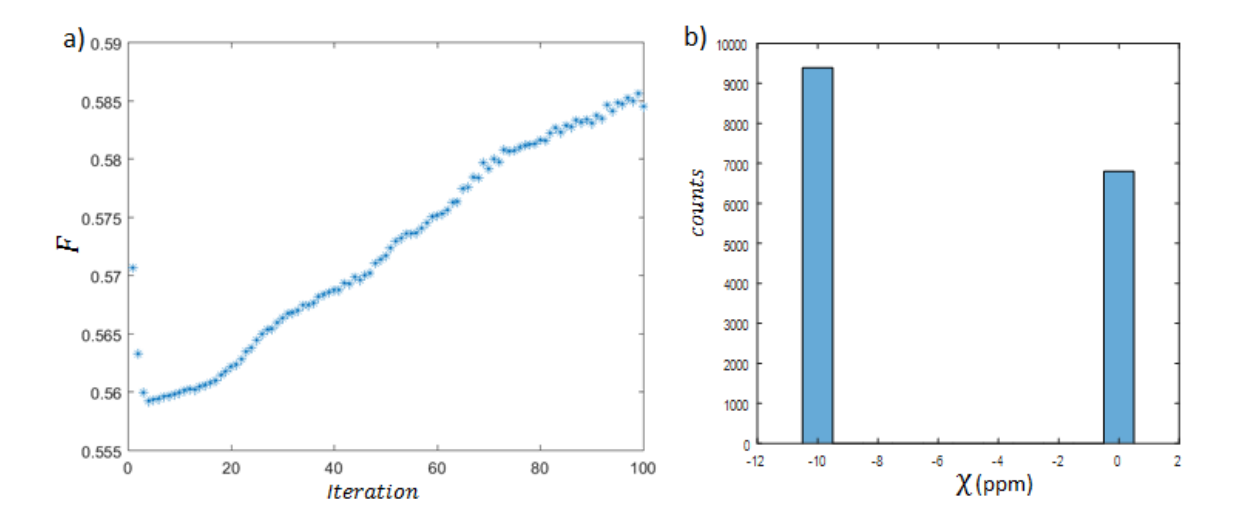


Fig. 4.8 (a) Cost function versus the number of iterations. The number of iterations is 100. (b) Histogram of the values of final magnetic susceptibility within the design domain: either zero or $\chi_{\text{target}} = -10$ ppm.

In the level set method, the cost function decreases for few iterations and then, it increases (4.8a). The increase in the cost function implies that the solution is not improving in every iteration, which may seem contradicting the good performance of the algorithm. However, there is an explanation to the behavior of the cost function: in every iteration we are reducing the epsilon, i.e., imposing gradually the constraints and forcing the algorithm to chose between fewer values in every iteration. This gradual enforcing of the constraints results in a decrease in F at the beginning (when the constraints are still quite loose) and in an increase in F once the constraints start playing a bigger role, which implies a less-effective solution. This clearly shows the trade off between effectiveness and practicality: the more constraints are imposed to the solution in order to be experimentally implementable, the more ineffective the solution becomes compared with the ideal case. So, although the cost function increases, the solution is optimized, but under the given constraints.

Figure 4.9 shows the B_0 field inhomogeneities before applying any correction (a), the magnetic field generated by the neck shim from the level set solution (b) and the final total magnetic field. The latter is the sum of the previous two. The solution of the level set algorithm homogenizes the B_0 field, but the perturbations are less corrected than when we use the LSQ solution, as expected. We are imposing constraints to the solution that highly restrict the values it can take. Hence, the final value of the cost function may be much higher than the 'ideal' least square solution. Nevertheless, the main field perturbations are sufficiently compensated.

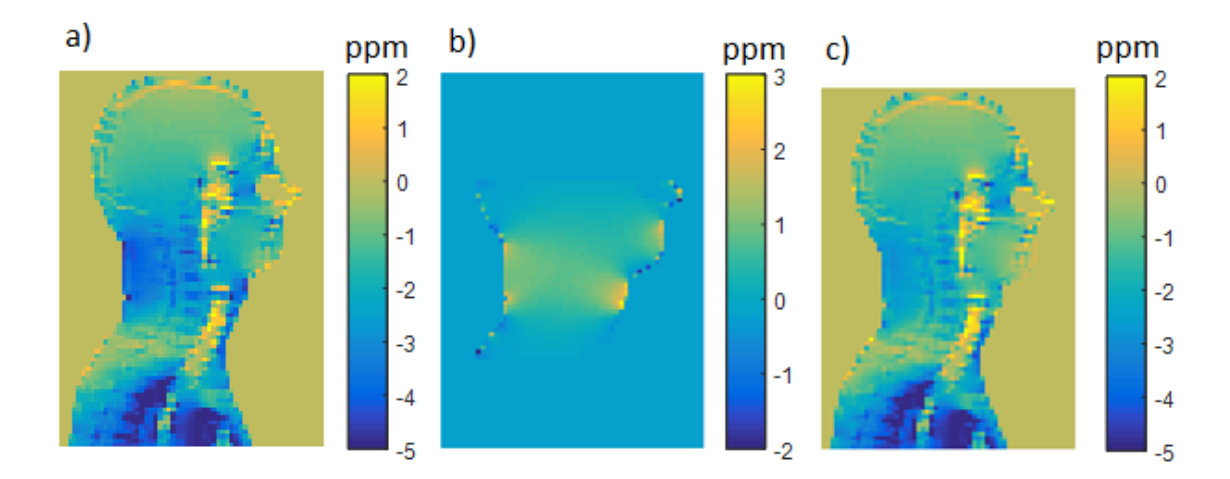


Fig. 4.9 (a) Magnetic field inhomogeneities produced by the human body. (b) Magnetic field produced by the level set solution for the neck shim, which should be able to compensate the inhomogeneities in the ROI. (c) Final magnetic field, which is the sum of the B_0 inhomogeneities generated by the human body and magnetic field generated by the level set solution for the neck shim.

In the following figure 4.10, we compare the final B_0 field correction along a line from the shoulders to the brain (as in figure 3.8), using the neck shim generated by the gradient descent algorithm and the one generated by the level set method. The inhomogeneities of the human body (blue line) are effectively corrected with the neck shim generated by the unconstraint gradient descent algorithm (yellow line). The level set method corrects the field inhomogeneities in a less effective way compared to the gradient descent minimization procedure. As mentioned before, this is expectable due to the highly restrictive constraints that we impose to the final solution.

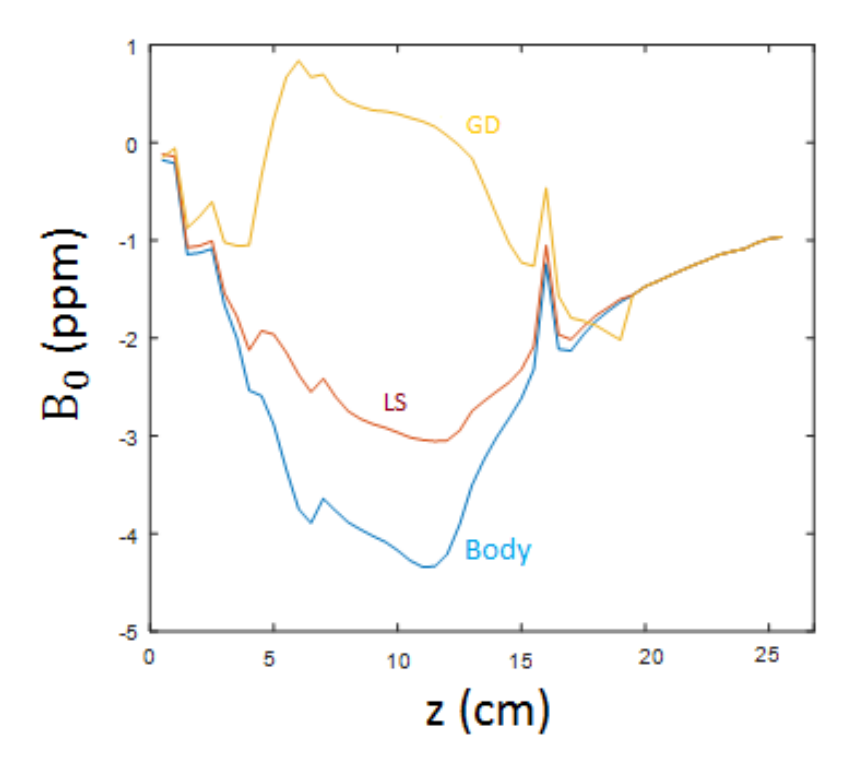


Fig. 4.10 B_0 field inhomogeneities along the z-direction, from the shoulders to the brain. The blue line represents the B_0 field disturbances of the human body without any correction. The yellow line is the final B_0 field after applying the neck shim generated by the gradient descent (GD) algorithm. The red line is the final B_0 field after applying the neck shim generated by the level set (LS) method.

The level set optimization integrated into the gradient descent algorithm allows us to have a solution for χ_f with only two values, thus forcing the algorithm to give a solution which is more practical. In our simulations, we find that the final values of χ_f lie within the given constraints. This characteristic makes the method a potentially useful tool for the design of shims to compensate the inhomogeneities of the B_0 field in the human body. However, our algorithm presents a main drawback: the final solution is dependent on the initial value of level set function. This happens to be a well-known problem that has been previously encountered in research on structural shape and topology optimization using level set methods [60]. The levels set method is a popular computational tool that optimizes structures defined by an implicit function, i.e., the level set function. In our algorithm, we use the direct approach to the level set based optimization, which is based on updating the level set function in every iteration, such that it advances towards an optimum. Even if the level set method is considered to be a powerful and flexible tool, the imposed constraints restrict the creation of new holes during the optimization. This can be a significant limitation for the robustness of the algorithm. Moreover, the given constraints harshly restrict the updates in the level set function and this can lead to the cost function getting stuck in a local minimum. This problem is stated in the book 'Topology Optimization' by Bendsøe and Sigmund: "In implementations, it is often seen that a too severe penalization of the intermediate density can lead to designs which are local minima and which are very sensitive to choice of the initial design for the iterative optimization procedure (one jumps too fast to a 0-1 design)" [61]. Various methods have been proposed to improve robustness in the level set topology optimization [60, 62, 63]. Due to time constraints, we could not further improve the algorithm and we leave this to future research, so that the best performance of the design optimization algorithm is attained.

All in all, we believe that the level set optimization integrated into a gradient descent algorithm can be a great approach to find the optimum design of shims to compensate the perturbations in the B_0 field in the human body. This algorithm could eventually provide us with a tool to find optimum designs of experimentally implementable PG foam shims that would be able to most efficiently homogenize the B_0 field in any ROI.

Chapter 5

Summary and Conclusion

In this thesis we have investigated the B_0 passive shimming approach of covering the skin with a magnetic susceptibility matching material from both an experimental and a mathematical viewpoint.

In the experimental study, we have demonstrated that a PG foam improves the uniformity of the B_0 field in a phantom and in vivo at 3T, thus confirming results from literature. We have derived the formula for the magnetic susceptibility of the PG foam, which is a function dependent on the volume fraction of both the PG microparticles and the bare foam. By fitting the experimental data to the formula, we have obtain the experimental values for the susceptibility of the PG powder and the susceptibility of the bare foam. Our values are in good agreement with theoretical values. Moreover, we have built a PG foam neck shim and we have compared the in vivo B_0 field maps with simulations: the experimental field corresponds well to the simulated one.

In the numerical study, we have presented an algorithm that aims to provide a solution to the topological optimization problem of finding an optimum design of a neck shim that efficiently homogenizes the B_0 field. The algorithm integrates the level set topology optimization method into a gradient descent minimization procedure. This algorithm imposes constraints to the design variable, thus providing a design which may be experimentally implementable as a PG foam for B_0 passive shimming. We show that the algorithm can be applied in the large-field-view that includes the neck and shoulders. The algorithm may further be improved by the implementation of hole insertion methods and other regularization techniques.

We believe that the level set method integrated into a gradient descent algorithm is a potential compelling approach to optimally design PG foams for passive B_0 shimming purposes. PG foams are simple to shape and lightweight, allowing for more complex designs than the magnetic susceptibility matching fluids. Therefore, we believe that the combination of a clever algorithm, which is able to give optimum designs, and the properties of PG foams, simple to shape and adjustable, could result in a great advance in the field of passive B_0 shimming.

Appendix A

The following function uses a level set method approach integrated into a gradient descent algorithm. The inputs of the function are the initial value of the level set function, χ_{target} , the Green's function, the desired B_0 field that the neck shim should create to obtain a final homogeneous B_0 field, infinitesimal elements in x and y direction for the integrals, epsilon, number of iterations, design domain and ROI domain. The last two functions are the smooth function for the Dirac-delta and the Heaviside function. The function gives two outputs: the final distribution of the magnetic susceptibility of the neck shim and the final value for the level set function.

```
function [chi, phi] = solve_levelset_Reinizialization3D(phi,
      targetchi, green, B0field, dx1, dx2, epsilon, nmax, maskshim, maskROI
  t=zeros(size(nmax));
   epsi=epsilon.^(1:nmax);
  A=green
  B=B0field
  FDin = zeros(1, nmax);
  dx = 0.005;
  dy = 0.005;
   dz = 0.005;
10
11
   for nin = 1:nmax
12
           epsilon = epsi(nin);
13
           % COMPUTE GRADIENT
15
           %this is gradient of the cost function
16
       gradient_phi = -targetchi*((A')*(A*(targetchi*
17
           approx_heaviside(phi, epsilon)) - B)).*approx_dirac(phi,
           epsilon);
18
19
      % FIND OPTIMAL STEPSIZE
20
21
```

```
beta = fminsearch (@(beta) object_inner_product (targetchi*
22
               A*approx_heaviside(phi + beta*gradient_phi, epsilon) -
                B, targetchi*A*approx_heaviside(phi + beta*
               gradient_phi, epsilon) - B, dx1, dx2), 0.1);
23
       % REINIZIALIZE
24
       temp=zeros(size(maskshim)); temp(maskshim)= phi;
25
       temp1 = maskshim == 0;
26
       temp2 = temp1 * (-10^{\circ}(9));
27
       temp3=temp+temp2;
28
29
       temp4=reinit_SD_3D (temp3, dx, dy, dz, 0.5, 'ENO3', 10); %
30
          method for reinizialization: reinit_SD_3D (Matlab Toolbox
           by B. Sumengen)
31
       phi=temp4 (maskshim);
32
33
           % UPDATE LEVEL—SET FUNCTION
34
       phi = phi + real(beta*gradient_phi);
35
36
       chi = targetchi*approx_heaviside(phi, epsilon);
37
       r = A*chi - B;
                               % object error
38
39
       FDin(nin) = object\_inner\_product(r, r, dx1, dx2);
40
   end
42
43
   function y = approx_heaviside(x, epsilon)
44
45
   if epsilon==0
46
       y = heaviside(x);
47
   else
48
       y = 0.5 + atan(x/epsilon)/pi;
49
  end
50
51
   function y = approx_dirac(x, epsilon)
52
   if epsilon==0
54
       epsilon = eps;
55
  end
56
  y = (1/pi)*epsilon./(epsilon^2 + x.^2);
```

Acknowledgements

I would like to thank Prof. dr. A. Webb and Dr. Wyger Brink for giving me the opportunity to do my final master internship in the C. J. Gorter center for High Field MRI.

I am particularly grateful to my daily supervisor Wyger, whose friendly support and encourage have continuously been present during these six months. Thanks to Wyger I have learned so much from a field I was new to and without him this thesis would not have been possible.

I would also like to thank Jying Dai for her help and friendship every day during my internship.

Finally, I want to express my very sincere gratitude to the most important people in my life: my parents. None of the accomplishments throughout my years of studies would have been possible without their unconditional love and support. Gracias.

Andrea Peña Darriba

Leiden, July 2017

Bibliography

- [1] MRI: A Peer-Reviewed, Critical Introduction. European Magnetic Resonance Forum (EMRF)/The Round Table Foundation (TRTF); A. P. Rinck (editor), 2016.
- [2] Image formation by induced local interactions: examples employing nuclear magnetic resonance. P. C. Lauterbur. Nature 242(5394):190-191, 1973.
- [3] MRI of the cervical nerve roots in the diagnosis of chronic inflammatory demyelinating polyradiculoneuropathy: a single-institution, retrospective case-control study. K. Tanaka, N. Mori, Y. Yokota, T. Suenaga. 3:e003443. 2013.
- [4] Simultaneous three-dimensional visualization of the intra-parotid facial nerve and parotid duct using a three-dimensional reversed FISP sequence with diffusion weighting. S. Naganawa, S. Ishihara, H. Satake, et al. Magnetic Resonance in Medical Science. 9:153–158, 2009.
- [5] Rapid high resolution MR neurography with a diffusion-weighted pre-pulse. M. Yoneyama, T. Takahara, T. C. Kwee, M. Nakamura, T. Tabuchi. Magnetic Resonance in Medical Science. 12:111–119., 2013.
- [6] Pyrolytic Graphite Foam: A Passive Magnetic Susceptibility Matching Material, G. C Lee, P. W. Goodwill, K. Phuong, B. A. Inglis, G. C. Scott, B. A. Hargreaves, L. Li, A. C. Chen, R. N. Shah and S. M. Conolly, J Magn Reson Imaging. 2010 Sep; 32(3): 684–691, 2010.
- [7] Diffusion-prepared neurography of the brachial plexus with a large field-of-view at 3T, J. Oudeman, B. F. Coolen, V. Mazzoli, M. Maas, C. Verhamme, W. M. Brink, A. G Webb, G. J. Strijkers, A. J. Nederveen, Journal of Magnetic Resonance Imaging., 43(3):644-54., 2015.
- [8] Improved frequency selective fat suppression in the posterior neck with tissue susceptibility matched pyrolytic graphite foam., G. Lee, C. Jordan, P. Tiet, C. Ruiz, J. Mc-Cormick, K. Phuong, B. Hargreaves, S. Conolly, J Magn Reson Imaging, 41(3):684-93, 2015.
- [9] Magnetic Resonance Technology: Hardware and System Component Design, The Roya Society of Chemistry 2016, New Developments in NMR No. 7, editted by Andrew G. Webb, 2016.

- [10] Magnetic resonance imaging: physical principles and sequence design., E. M. Hacke. New York: Wiley; 1999. XXVII, 914.
- [11] Principles of magnetic resonance imaging, D. G. Nishimura. 2010.
- [12] Quantum Mechanics, E. Merzbacher, 3rd ed., John Wiley, 1998.
- [13] Spin Dynamics, M. H. Levitt, John Wiley and Sons Ltd., 2008.
- [14] The Effect of Magnetisation on the Nature of Light Emitted by a Substance, P. Zeeman, Nature. 55 (1424): 347., 1897.
- [15] The Nuclear Induction experiment, F. Bloch, W. W. Hansen and M. Packard, Physical Review Letter, 69, 127, 1946.
- [16] Magnetic susceptibility measurement of insoluble solids by NMR: magnetic susceptibility of bone., J. A. Hopkins, F. W. Wehrli. Magnetic Resonance Medicine;37:494–500: 1997.
- [17] Numerical calculations of the static magnetic field in three-dimensional multi-tissue models of the human head, C. M. Collins, B. Yang, Q. X. Yang, M. B. Smith. Magnetic Resonance Imaging;20:413–424, 2002.
- [18] Strategies for shimming the breast. N. Maril, C. M. Collins, R. L. Greenman, R. E. Lenkinski. Magnetic Resonance Medicine.;54:1139–1145. 2005.
- [19] The Virtual Family Development of Surface Based Anatomical Models of two Adults and two Children for Dosimetric Simulations, A. Christ, W. Kainz, E. G. Hahn, K. Honegger, M.Zefferer, E. Neufeld, W. Rascher, R. Janka, W. Bautz, J. Chen, B. Kiefer, P. Schmitt, H. P. Hollenbach, J. X. Shen, M. Oberle, D. Szczerba, A. Kam, J. W. Guag, and N. Kuster. Physics in Medicine and Biology, vol. 55, N23, 2010., S. K. Lee, I. Hancu, Journal of Magnetic Resonance Imaging 36:873-880, 2012.
- [20] A Fast Calculation Method for Magnetic Field Inhomogeneity due to an Arbitrary Distribution of Bulk Susceptibility, R. Salomir, B. D. de Senneville and C. T. W. Moonen, Concepts in Magnetic Resonance part B (Magnetic Resonance Engineering), Vol. 19B(1) 26-34, 2003.
- [21] Application of Fourier-Based Method for rapid Calculation of Filed Inhomogeneity Due to Spatial Variation of Magnetic Susceptibility, J. P. Marques and R. Bowtell, Concepts in Magnetic Resonance part B (Magnetic Resonance Engineering), Vol. 25B(1) 65-78, 2005.
- [22] Volume of interest-based Fourier Transform method for calculation of static magnetic field maps from susceptibility distributions, R. Dewal, Q. X. Yang, Magnetic Resonance in Medicine 75:2473–2480, 2016.

- [23] Dynamic shim updating: A new approach towards optimized whole brain shimming. Magnetic Resonance in Medicine, A. M. Blamire, D. L. Rothman, T. Nixon, 36(1):159–165, 1996.
- [24] Rapid in vivo proton shimming. Magnetic Resonance in Medicine., E. Schneider, G. Glover, 18(2):335–347, 1991.
- [25] Fast, Fully Automated Global and Local Magnetic Field Optimization for fMRI of the Human Brain., J. L. Wilson, M. Jenkinson, I. de Araujo, M. L. Kringelbach, E. T. Rolls, P. Jezzard, Neuroimage, 17(2):967–976, 2002.
- [26] Reducing Magnetic-Susceptibility Differences Using Liquid Fluorocarbon Pads (Sat Pad(Tm)) Results with Spectral Presaturation of Fat. Artificial Cells Blood Substitutes and Immobilization Biotechnology., S. S. Eilenberg, V. M. Tartar, R. F. Mattrey, 22(4):1477–1483, 1994.
- [27] 3T MR of the prostate: Reducing susceptibility gradients by inflating the endorectal coil with a barium sulfate suspension., Y. Rosen, B. N. Bloch, R. E. Lenkinski, R. L. Greenman, R. P. Marquis, N. M. Rofsky, Magnetic Resonance in Medicine, 57(5):898–904, 2007.
- [28] Pyrolytic carbon. In Biomaterials science: an introduction to materials in medicine., Ratner, D. Buddy, Academic Press. p. 171-180, 2004.
- [29] Anisotropic Thermal Conductivity of Pyrolytic Graphite, G. A. Slack, Physical Review, 127(3):694., 1962.
- [30] Superhard conductive carbon nanocrystallite films., S. Hirono, S. Umemura, M. Tomita, R. Kaneko, Applied Physics Letters, 80(3):425–427, 2002.
- [31] Schenck JF. The role of magnetic susceptibility in magnetic resonance imaging: MRI magnetic compatibility of the first and second kinds., Medical Physics., 23(6):815–850, 1996
- [32] Magnetic properties of materials fro MRI engineering, micro-MR and beyond., Journal of Magnetic Resonance, Matthias C Wapler, Jochen Leupold, Iulius Dragonu, Dominik von Elverfeld, Maxim Zaitsev, Ulrike Wallrabe 242C, 233-242, 2014.
- [33] Biomedical magnetic resonance technology. C. N. Chen, D. I. Hoult. Bristol: Adam Hilger, 2005.
- [34] Optical Metamaterials: Fundamentals and Applications, C. Wenshan; V. Shalaev, Optical Metamaterials: Fundamentals and Applications. Springer. pp. Chapter 2.4., 2009.
- [35] Predictions of effective physical properties of complex multiphase materials, M. Jump up Wang, N. Pan, Materials Science and Engineering: R: Reports. 63: 1., 2008.

- [36] AC and dc conductivity-based microstructural characterization., D. S. McLachlan, Cai K, G. Sauti, International Journal of Refractory Metals and Hard Materials, 19(4-6):437-445., 2001.
- [37] Inherently conducting polymer modified polyurethane smart foam for pressure sensing., S. Brady, D. Diamond, K-T. Lau., Sensors and Actuators A: Physical., 119(2):398–404., 2015.
- [38] Electrical Resistivity of Composites, D. S. McLachlan, M. Blaszkiewicz, R. E. Newnham., Journal of the American Ceramic Society., 73(8):2187–2203., 1990.
- [39] A theoretical approach based on electromagnetic scattering fro analysing dielectric shimming in hish-field MRI., W. M. Brink, R. F. Remis, A. G. webb, Magnetic resonance in medicine, 75:2185-2194, 2016.
- [40] Patient-to-patient variation of susceptibility-induced B0 field in bilateral breast MRI,
 S. K. Lee, I. Hancu, Journal of Magnetic Resonance Imaging 36:873-880, 2012.
- [41] The Fourier Transform and Its Applications, R. Bracewall, McGraw-Hill (2nd edition), 1986.
- [42] Rapid calculations of susceptibility-induced magnetostatic field perturbations for in vivo magnetic resoance, K. M. Koch, X. Papademetris, D.L. Rothman, R. A. de Graaf. Physical Medical Biology, 51:6381-6402, 2006.
- [43] Subject-specific models of susceptibility-induced B0 field variations in breast MRI, C. D. Jordan, B. L. Daniel, K. M. Koch, H. Yu, S. Conolly, B. A. Hargreaves. Journal of Magnetic Resonance Imaging, 37: 227-231, 2013.
- [44] Fronts propagating with curvature-dependent speed: Algorithms based on Hamilton-Jacobi formulations, S. Osher, J. A. Sethian, Journal of Computational Physics. 79, 12-49, 1998.
- [45] Level set methods for inverse scattering, O. Dorn and D. Lesselier, vol. 22, pp. R67-R131, 2006.
- [46] Microwave medical imaging using level set techniques, N. Irishna, PhD thesis., 2009.
- [47] An introduction to optimization, K. P. Chong, S. H. Zak. A Wiley-Interscience Publication JOHN WILEY and SONS, INC. 2nd edition, 2001.
- [48] A level-set approach for inverse problems involving obstacles, F. Santosa, Control, optimization and calculus of variations. !:17-33. 1996.
- [49] XFEM schemes for level set based structural optimization, L. Li, M. Y. Wang, P. Wei, Frontiers of Mechanical Engineering., Vol. 7 Issue (4): 335-356., 2012.

- [50] A Review of Statistical Approaches to Level Set Segmentation: Integrating Color, Texture, Motion and Shape, D. Cremers, International Journal of Computer Vision 72(2), 195–215, 2007.
- [51] Optimization methods in electromagnetic radiation, Springer-Verlag, New York, USA, 2004.
- [52] Non-invasive electromagnetic ablation of female breast tumors, Msc Thesis, W. M. Brink.
- [53] Level Set Methods and Dynamic Implicit Surfaces Authors, S. Osher, F. Ronald., 2003.
- [54] Level Set Methods and Fast Marching Methods Evolving Interfaces in Computational Geometry, Fluid Mechanics, Computer Vision, and Materials Science, J. A. Sethian, Cambridge University Press, Cambridge Monograph on Applied and Computational Mathematics., 1999.
- [55] A level set approach for computing solutions to incompressible two-phase flow, M. Sussman, P. Smereka, S. Osher. Journal of computational physics. 114: 146-159, 1996.
- [56] A survey on level set methods for inverse problems and optimal design, M. Burger, S. J. Osher. 2004.
- [57] A survey on multiple level set methods with applications for identifying piecewise constant functions, X-C. Tai and F. C. Tony, International Journal of Numerical Analysis Modeling, 1(1), 25-47, 2004.
- [58] Tissue magnetic susceptibility matched pyrolytic graphite foam for improved MRI, G.C. Lee. PhD Thesis, 2011.
- [59] A Matlab toolbox implementing Level Set Methods., Baris Sumengen, vision research lab at UC Santa Barbara. 2005.
- [60] A new hole insertion method for level set based structural topology optimization, P. D. Dunning and H. A. Kim, International Journal for Numerical Methods in Engineering, 93 (1), pp. 118-134, 2013.
- [61] Topology Optimization. Theory, methods and applications, M. P. Bendsøe, O. Sigmund, 2003.
- [62] Incorporating topological derivatives into level set methods., M. Burger, B. Hackl, W. Ring. Journal of Computational Physics; 194(1):344-362. 2004.
- [63] Incorporating topological derivatives into shape derivatives based level set methods, L. He, C-Y. Kao, S. Osher. Journal of Computational Physics; 225(1):891-909, 2007.